



HAL
open science

Updated Radiative Transfer Model for Titan in the Near-infrared Wavelength Range: Validation against Huygens Atmospheric and Surface Measurements and Application to the Cassini/VIMS Observations of the Dragonfly Landing Area

M Es-Sayeh, S Rodriguez, Maélie Coutelier, Pascal Rannou, B Bézard, L Maltagliati, T Cornet, B Grieger, E Karkoschka, S Le Mouélic, et al.

► **To cite this version:**

M Es-Sayeh, S Rodriguez, Maélie Coutelier, Pascal Rannou, B Bézard, et al.. Updated Radiative Transfer Model for Titan in the Near-infrared Wavelength Range: Validation against Huygens Atmospheric and Surface Measurements and Application to the Cassini/VIMS Observations of the Dragonfly Landing Area. *The Planetary Science Journal*, 2023, 4, pp.44. 10.3847/psj/acbd37 . insu-04036493

HAL Id: insu-04036493

<https://insu.hal.science/insu-04036493>

Submitted on 19 Mar 2023

HAL is a multi-disciplinary open access archive for the deposit and dissemination of scientific research documents, whether they are published or not. The documents may come from teaching and research institutions in France or abroad, or from public or private research centers.

L'archive ouverte pluridisciplinaire **HAL**, est destinée au dépôt et à la diffusion de documents scientifiques de niveau recherche, publiés ou non, émanant des établissements d'enseignement et de recherche français ou étrangers, des laboratoires publics ou privés.



Distributed under a Creative Commons Attribution 4.0 International License



Updated Radiative Transfer Model for Titan in the Near-infrared Wavelength Range: Validation against Huygens Atmospheric and Surface Measurements and Application to the Cassini/VIMS Observations of the Dragonfly Landing Area

M. Es-sayeh¹, S. Rodriguez¹, M. Coutelier², P. Rannou³, B. Bézard⁴, L. Maltagliati⁵, T. Cornet⁶, B. Grieger⁶, E. Karkoschka⁷, S. Le Mouélic⁸, A. Le Gall⁹, C. Neish¹⁰, S. MacKenzie¹¹, A. Solomonidou¹², C. Sotin⁸, and A. Coustenis⁴

¹ Université Paris Cité, Institut de physique du globe de Paris (IPGP), CNRS, Paris, France; essayeh@ipgp.fr

² LATMOS/IPSL, UVSQ Université Paris-Saclay, Sorbonne Université, CNRS, Guyancourt, France

³ Groupe de Spectrométrie Moléculaire et Atmosphérique, UMR CNRS 7331, Université de Reims Champagne-Ardenne, Reims, France

⁴ LESIA, Observatoire de Paris, Université PSL, CNRS, Sorbonne Université, Université Paris Cité, 5 place Jules Janssen, F-92195, Meudon, France

⁵ Nature Astronomy, Springer Nature, 4 Crinan Street, London N1 9XW, UK

⁶ Aurora Technology B.V. for ESA—European Space Agency, European Space Astronomy Centre (ESAC), Camino Bajo del Castillo s/n, Urb. Villafranca del Castillo, E-28692 Villanueva de la Cañada, Madrid, Spain

⁷ Lunar and Planetary Laboratory, 1629 E University Boulevard, Tucson, AZ 85721-0092, USA

⁸ Laboratoire de Planétologie et Géosciences, CNRS UMR 6112, Nantes Université, Université d'Angers, Université du Mans, Nantes, France

⁹ Laboratoire Atmosphères, Milieux, Observations Spatiales (LATMOS), UVSQ/CNRS/Paris VI, UMR 8190, F-78280 Guyancourt, Institut Universitaire de France (IUF), Paris, France

¹⁰ Department of Earth Sciences, The University of Western Ontario, London, ON N6A 5B7, Canada

¹¹ Johns Hopkins University Applied Physics Laboratory, 11100 Johns Hopkins Road, Laurel, MD 20723, USA

¹² Hellenic Space Center, Athens, Greece

Received 2022 October 17; revised 2023 February 17; accepted 2023 February 18; published 2023 March 14

Abstract

We present an analysis of Titan data acquired by the Cassini Visual and Infrared Mapping Spectrometer (VIMS) at the landing site of the Dragonfly mission, using a new version of our radiative transfer model for Titan, with significant updates for the spectroscopic parameters of atmospheric gases and photochemical aerosols. Our updated radiative transfer model is validated against the in situ spectroscopic measurements of the Huygens probe during its descent and once landed. We confirm that aerosols with a fractal dimension of 2.3–2.4 provide the best fit to the observations. We apply our radiative transfer model to four VIMS data cubes over the Selk crater region including the Dragonfly landing and exploration areas, further validating our model by producing consistent aerosol population and surface albedo maps. These infrared albedo maps, further corrected from the photometry, enable us to study the Selk crater region in terms of surface composition, landscape formation, and evolution. Our results suggest that the Selk crater is in an intermediate state of degradation and that the mountainous terrains of the area (including the crater rim and ejecta) are likely to be dominated by fine grains of tholin-like sediment. This organic sediment would be transported to the lowlands (crater floor and surrounding plains), possibly with water ice particles, by rivers, and further deposited and processed to form the sand particles that feed the neighboring dune fields. These results provide information for the operational and scientific preparation of the Dragonfly mission, paving the way for future exploration of Titan's surface composition and geology.

Unified Astronomy Thesaurus concepts: Titan (2186); Radiative transfer (1335); Near infrared astronomy (1093); Planetary atmospheres (1244); Planetary surfaces (2113)

1. Introduction

Titan is the largest icy moon of Saturn. It is the only moon in the solar system with a thick atmosphere, dominated by nitrogen and methane. Energetic atmospheric chemistry driven by solar ultraviolet photons and solar wind particles accelerated by Saturn's magnetosphere leads to the production of a plethora of complex organic molecules, including prebiotic progenitors, that form a ubiquitous layer of organic aerosols. Most of the heaviest molecules produced in the atmosphere, along with aerosols, continuously settle down to the surface (e.g., Flasar 1983; Lunine et al. 1983; Yung et al. 1984; Malaska et al. 2016), possibly resulting in a layer of organic sediment up to tens of meters thick. In addition, at the

cryogenic temperature of Titan's surface (≈ 90 – 94 K) and deepest atmosphere, methane and ethane, the most volatile atmospheric compounds, participate in climatic cycles similar to the hydrological cycle on Earth, with clouds, rain, and stable liquid areas at the surface. As a complex, active world dominated by water ice and organic molecules, Titan is a prime target for planetary and astrobiological research.

The surface of Titan is subject to geological processes (e.g., aeolian and fluvial erosion) that lead to the formation of a variety of landscapes, including dune fields, river networks, mountains, labyrinth terrains, canyons, lakes, and seas (e.g., Lopes et al. 2019), analogous to their terrestrial counterparts but in an exotic context. The analysis of Titan's surface reflectivity in the near-infrared (NIR) has the potential to help estimate the surface composition, which in turn can help us understand the processes leading to the formation and evolution of Titan's landscapes. Titan's optically thick atmosphere, however, prevents the surface from being probed from orbit



Original content from this work may be used under the terms of the [Creative Commons Attribution 4.0 licence](https://creativecommons.org/licenses/by/4.0/). Any further distribution of this work must maintain attribution to the author(s) and the title of the work, journal citation and DOI.

in the entirety of the NIR range, and its composition is still largely unknown and debated, preventing us from fully understanding and quantifying the geological processes at play. Incident and reflected solar radiations are indeed strongly affected by gaseous absorption and aerosol scattering in the visible and NIR. Only where the methane absorption is weak enough do a few transmission windows give access to the detection of radiation reflected by the low atmosphere and the surface, making possible the retrieval of the surface albedo. In the 0.88–5.11 μm range (NIR channel), the Visual and Infrared Mapping Spectrometer (VIMS) instrument on board the Cassini spacecraft (Brown et al. 2004) has shown that the surface can be observed in eight narrow transmission windows centered at 0.94, 1.07, 1.28, 1.58, 2.02, 2.70, and 2.78 μm and in the 4.89–5.13 μm interval (Sotin et al. 2005). Even in these transmission windows, residual gaseous absorption and increasing aerosol scattering with decreasing wavelength make the analysis of the surface signal and the retrieving of surface albedo complex.

In order to retrieve the surface albedo in the atmospheric windows, we apply a radiative transfer (RT) model to simulate the radiance factor (I/F) in the NIR channel of Cassini/VIMS observations of Titan. RT models in the NIR for Titan have been developed for decades (e.g., McKay et al. 1989; Griffith et al. 1991, 2003, 2012; Rannou et al. 1995, 2003, 2016, 2021; Ádámkóvics et al. 2004, 2009, 2016; Adriani et al. 2005; Negrão et al. 2006; Hirtzig et al. 2013; Barnes et al. 2018; Corlies et al. 2021; Coutelier et al. 2021), progressively upgrading the optical properties of atmospheric gases and photochemical aerosols and improving the robustness of Titan’s radiative budget estimation and surface albedo retrievals. We developed in our team an RT model for Titan based on the model of Hirtzig et al. (2013). Our model has known a few upgrades (Maltagliati et al. 2015b; Cornet et al. 2017) since the first version, and a complete description of the penultimate version is available in the supplementary material of Rodriguez et al. (2018). Taking advantage of recent significant advances in molecular spectroscopy relevant to Titan’s atmospheric gases (Rey et al. 2018) and of a new paradigm for the description of Titan’s aerosols optical properties (Coutelier et al. 2021; Rannou et al. 2022), we recently undertook the realization of several major improvements to our model, which will be detailed in this article.

In this article, we first present the details of our RT model and its major updates since its previous version. We will then describe our tests to validate this new model against in situ Huygens measurements, both during its entire descent sequence and once landed. We will compare our validation results with those of the previous iteration of the model. Once our new model is validated, we will apply it to the Dragonfly landing area, in a region a few hundreds of kilometers wide, centered on the Selk crater, in order to extract the surface albedo over the entire area and discuss the regional spectral heterogeneities and their possible links to the local geomorphology.

2. Description of the New IPGP RT Model for Titan

In this section, we present the most recent evolution of the radiative transfer model for Titan developed at IPGP (Institut de Physique du Globe de Paris) team.

2.1. The Baseline of Our RT Model (RT-IPGP-2016), General Comments on Validity Domains and Accuracy Trade-offs

The general architecture of our RT model for Titan is directly inherited from the model presented in detail in Hirtzig et al. (2013), including a few, but significant updates regarding the gas and aerosol descriptions, leading to a version that stabilized in 2016 (Maltagliati et al. 2015a; Cornet et al. 2017; Rodriguez et al. 2018), hereafter referred to as RT-IPGP-2016 and summarized in Table 1. In the model, Titan’s atmosphere is divided into 70 layers extending from the surface up to 700 km altitude. Pressure and temperature at boundary altitude levels are taken from Cassini-CIRS (Composite Infrared Spectrometer) measurements (Vinatier et al. 2010) at the latitude of Huygens. We include atmospheric opacity sources from gases—Rayleigh scattering from nitrogen (N_2) and methane (CH_4); collision-induced absorption by nitrogen and hydrogen (H_2); and absorption by methane, its isotopologues $^{13}\text{CH}_4$ and CH_3D , acetylene (C_2H_2), and carbon monoxide (CO)—and photochemical aerosols. Molecular line lists for gaseous methane and its isotopologues have been compiled over the whole spectral range of the VIMS infrared channel (0.88–5.11 μm) from laboratory measurements, theoretical calculations, and empirical models (all the corresponding references can be found in Hirtzig et al. 2013). Line lists for acetylene and carbon monoxide are taken from the GEISA2009 database (Jacquinet-Husson et al. 2011). Correlated- k absorption coefficients have been computed for all the gaseous species at the VIMS spectral sampling, on a “pressure–temperature” grid defined by the Huygens and Cassini measurements, with line profiles and cutoffs recommended by De Bergh et al. (2012). Concerning the aerosols, we use as a reference the phase functions, single-scattering albedos, and vertical extinction profiles constrained by the Huygens/DISR instrument (Tomasko et al. 2008; Doose et al. 2016), extrapolated in wavelengths to the VIMS infrared range. In order to account for the seasonal and latitudinal variability of the haze content, we allow the reference aerosol extinction profile to be freely multiplied by a uniform scaling factor. Finally, a Lambertian surface is assumed. Given an input surface and atmospheric model, the radiative transfer calculation is performed via the plane-parallel version of the Spherical Harmonic Discrete Ordinate Method solver (SHDOMPP; Evans 2007) or via the C-code version of the Discrete Ordinates Radiative Transfer Program in pseudo-spherical geometry (SPS-DISORT; Buras et al. 2011), depending on the incidence angle domain.

The choice of the RT solver (SHDOMPP or SPS-DISORT) depends on the incidence angle. Barnes et al. (2018) consider the use of the plane-parallel approximation—faster than with a pseudo-spherical approximation—acceptable up to 60° incidence. Following the Coutelier et al. (2021) tests, differences between I/F calculated with SHDOMPP and SPS-DISORT at incidence angles above 60° are greater than 5% and below 3% at incidence angles lower than 50°. We thus recommend using the plane-parallel approximation up to 50° incidence angle and to switch to pseudo-spherical geometry above. As SPS-DISORT does not take into account the pseudo-spherical geometry for the emission angle direction, it should not be used at an emission angle higher than 60°, unfortunately limiting the usable observations to a narrower range of observation angles than available.

Finally, RT solvers calculate the intensity field for a finite number of polar and azimuth angles—so-called streams—for

Table 1
Models' Atmospheric Inputs

Model	RT-IPGP-2022	RT-IPGP-2016
Grid	0–700 km with 10 km layers	0–700 km with 10 km layers
Temperature–pressure profile	Huygens/HASI (Fulchignoni et al. 2005)	Cassini/CIRS (Vinatier et al. 2010)
Gas VMR		
CH ₄	0–80 km: Huygens/GCMS (Niemann et al. 2010) 80–350 km: linearly interpolated to 1% 350–700 km: constant at 1%	0–140 km: Huygens/GCMS (Niemann et al. 2010) constant above (1.48%)
D/H	ALMA (Thelen et al. 2019)	Cassini/CIRS (Bézard et al. 2007)
¹³ C/ ¹² C	ALMA (Serigano et al. 2016)	Cassini/GCMS (Niemann et al. 2010)
CO	ALMA (Serigano et al. 2016)	De Kok et al. (2007)
C ₂ H ₂	Cassini/CIRS (Vinatier et al. 2007) constrained at low altitude with saturation curve	Cassini/CIRS (Vinatier et al. 2010)
HCN	ALMA (Thelen et al. 2019)	None
Gas absorption		
CH ₄	TheoReTS (Rey et al. 2018)	<1.263 μm: Karkoschka & Tomasko (2010) 1.263–1.71 μm: Campargue et al. (2012) <1.71 μm: calculated as described in Albert et al. (2009) and Boudon et al. (2006) ¹² CH ₄ and ¹³ CH ₄ : line lists from Nikitin et al. (2002) CH ₃ D: line lists from Nikitin et al. (2006, 2013)
C ₂ H ₂	Hitran (Rothman et al. 2013)	GEISA2009 (Jacquinet-Husson et al. 2011)
CO	Hitran (Rothman et al. 2013)	GEISA2009 (Jacquinet-Husson et al. 2011)
HCN	Hitran (Rothman et al. 2013)	None
Collision-induced absorption	N ₂ –N ₂ and N ₂ –H ₂ (Lafferty et al. 1996; McKellar 1989) using a constant 0.1% H ₂ VMR (Niemann et al. 2010)	N ₂ –N ₂ and N ₂ –H ₂ (Lafferty et al. 1996; McKellar 1989)
Rayleigh scattering (based on the refractive index fitted by equations available in Sneepe & Ubachs 2005)	CH ₄ : Loria (1909) on 0.53–0.66 μm, Rollefson & Havens (1940) on 1.68–14.8 μm, interpolated over the VIMS-IR wavelength range, King correction from Bates (1984) N ₂ : Peck & Khanna (1966) on 0.5–2.06 μm, extrapolated over the VIMS-IR wavelength range, King correction from Naus & Ubachs (2000) C ₂ H ₂ : Loria (1909) on 0.546–0.670 μm, extrapolated over the VIMS-IR wavelength range CO: Smith et al. (1976) on 0.168–0.288 μm, extrapolated over the VIMS-IR wavelength range	CH ₄ : Loria (1909) on 0.53–0.66 μm, extrapolated over the VIMS-IR wavelength range N ₂ : Peck & Khanna (1966) on 0.5–2.06 μm, extrapolated over the VIMS-IR wavelength range
Aerosols		
Refractive indices	Khare et al. (1984) modified by Rannou et al. (2010)	Not needed
Phase function	Haze: Fractal aggregate model (Rannou et al. 2003) modified following S. Rodriguez et al. (2023, in preparation) Mist: Fractal aggregate model (Rannou et al. 2003) modified following S. Rodriguez et al. (2023, in preparation)	Doose et al. (2016)
Single-scattering albedo	Fractal aggregate model (Rannou et al. 2003) for $z > 200$ km, with (Doose et al. 2016) altitude dependency below	Doose et al. (2016)
Extinction profile	Fractal aggregate model (Rannou et al. 2003; Coutelier et al. 2021)	Doose et al. (2016)

each atmospheric layer defined in the model. The higher the number of streams is, the higher are the accuracy and the computation time. Sixteen polar streams are used for both

solvers. Following Coutelier et al. (2021), the number of streams in azimuth at wavelengths lower than 1.7 μm is set to 32 and 40 for SHDOMPP and SPS-DISORT, respectively.

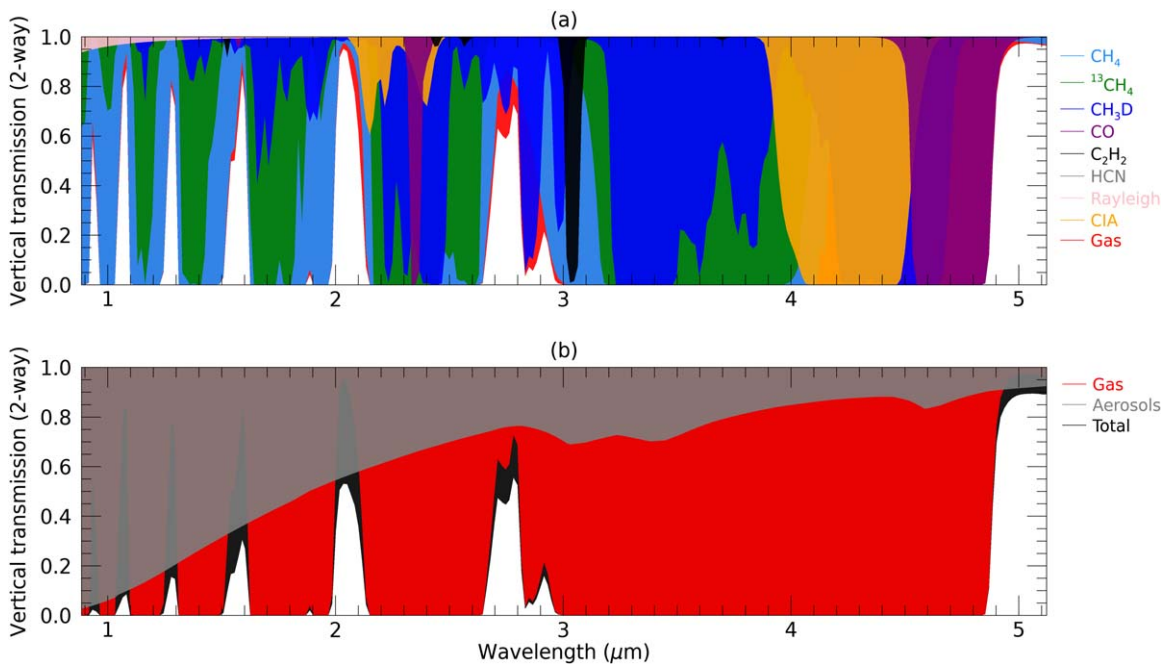


Figure 1. Two-way vertical transmission as a function of the wavelength as calculated by the RT-IPGP-2022 model. (a) Gas contributions only. (b) Total, all gases, and aerosol contributions.

Twenty-four streams in azimuth are used for both solvers at larger wavelengths. It should be noted that, for incidence angles higher than 80° , 32 streams in azimuth are used beyond $1.7 \mu\text{m}$. Doing so, less than 0.5% differences in I/F are produced when compared to a test case using a very high angular resolution, such as 100 streams (Coutelier et al. 2021).

2.2. Summary of the Most Recent Updates of Our RT Model (RT-IPGP-2022)

Built on the RT-IPGP-2016 iteration, the present up-to-date version of our RT model, called RT-IPGP-2022 hereafter, is presented in detail below. Figure 1 summarizes the relative contribution of all the atmospheric input absorption and scattering sources of the RT-IPGP-2022 model to Titan's simulated atmospheric transmission.

2.2.1. Titan's Climatology and Gaseous Abundances

A first upgrade of our RT model concerns atmospheric structure and composition. In order to be fully consistent with the reference atmospheric structure used to calculate the gas absorption coefficients, pressure and temperature at boundary altitude levels are now taken from Huygens-HASI (Huygens Atmospheric Structure Instrument) measurements (Fulchignoni et al. 2005). Vertical profiles of the volume mixing ratio (VMR) and isotopic ratios for our catalog of gases have been updated using the values from the most recent studies. A constant carbon monoxide VMR of 49.6 ppm is set following the recommendation of Serigano et al. (2016). Acetylene, the third most abundant unsaturated hydrocarbon in Titan's atmosphere, is considered with a stratospheric VMR following the Cassini-CIRS analyses of Vinatier et al. (2007) and constant above their highest altitude value—480 km. As it condenses at ≈ 70 km, the profile is adapted following the acetylene saturation curve. From the surface up to 80 km, we use the Niemann et al. (2010) methane VMR, linearly interpolated to 1% at 350 km following Yelle et al. (2021),

and constant up to the highest grid level. Hydrogen cyanide (HCN), the simplest and most abundant nitrile, has been added to our gases database, and its VMR is set using the most recent profile of Thelen et al. (2019) and linearly extrapolated above their highest altitude value. D/H and $^{12}\text{C}/^{13}\text{C}$ isotopic ratios were set to the most recent observations with ALMA (Atacama Large Millimeter/submillimeter Array), which are $1.033 \cdot 10^{-4}$ (Thelen et al. 2019) and $89.9 \cdot 10^{-5}$ (Serigano et al. 2016), respectively.

The temperature–pressure and gas VMR profiles are input parameters that are fixed in our model. Since observations have shown that they can vary both seasonally and/or spatially, we quantified the effect of their largest variation range on the simulated I/F spectra. This is illustrated in Figure 2 by showing the relative difference between the simulated I/F with the recommended profile (Table 1, middle column) and the one computed with the most extreme case, for each considered parameter. All spectra are simulated under the same geometry and configuration (i.e., observation angles to 0° , surface albedo set to 0 and aerosol scaling factors set to one relatively to the aerosol opacity observed by Doose et al. 2016).

From the surface up to the tropopause (≈ 48 km, corresponding to the ≈ 100 mbar level), temperatures of roughly 5 K colder than the recommended values have been observed (Anderson et al. 2014; Lellouch et al. 2014; Jennings et al. 2019; Schinder et al. 2020). Higher in altitude, the general trend is that the temperature can diminish by ≈ 15 K, still with respect to the recommended values (Vinatier et al. 2010, 2015, 2020; Coustenis et al. 2016, 2020; Teanby et al. 2017, 2019; Mathé et al. 2020; Sylvestre et al. 2020; Rannou et al. 2022). We show in Figure 2 the relative difference between the I/F simulated with the recommended temperature profile and the profile decreased by 15 K above 120 km and by 5 K below 50 km.

Although very localized variations (confined at certain altitudes) of the VMR of CH₄ have been reported (Lellouch et al. 2014), they have no impact on our modeling, unlike more

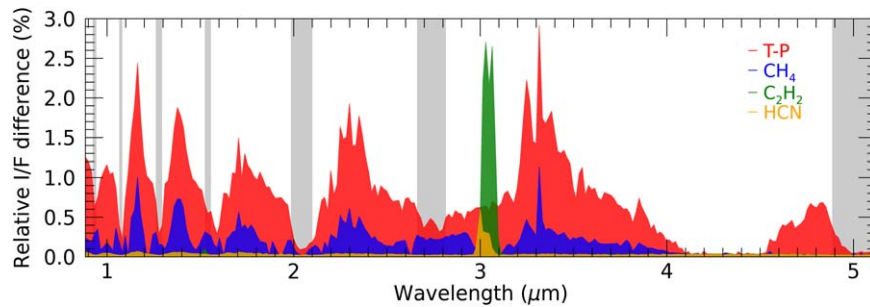


Figure 2. Relative I/F differences between RT-IPGP-2022 simulations with recommended and modified atmospheric input parameters for the T - P profile and CH_4 , C_2H_2 , and HCN VMR. Atmospheric transmission windows are shaded in gray.

globally distributed variations of the profile. The general trend is that the tropospheric methane abundance can globally decrease by $\approx 10\%$ relative to the recommended abundance profile (Penteado & Griffith 2010; Ádámkóvics et al. 2016) and the stratospheric methane abundance can increase globally by $\approx 10\%$, still relative to the recommended profile (Rannou et al. 2022). We show in Figure 2 the relative difference between the simulated I/F with the recommended methane profile and decreased by 10% below 10 km and increased by 10% above the 190 km altitude.

The VMR of C_2H_2 can vary by a factor of ≈ 4 above 120 km altitude and the VMR of HCN by a factor of ≈ 15 above 120 km altitude, both around the recommended profile (Vinatier et al. 2010, 2015, 2020; Coustenis et al. 2016, 2020; Maltagliati et al. 2015a; Teanby et al. 2017, 2019; Mathé et al. 2020). When decreasing or increasing the VMR of HCN and C_2H_2 by the same amount, their relative differences remain identical with wavelengths, except at wavelengths of their major absorption bands near $3 \mu\text{m}$, where the relative difference is smaller when decreasing the VMR. Being conservative, we thus show in Figure 2 the relative difference between the simulated I/F with the recommended HCN and C_2H_2 profiles, and the same profiles increased above 120 km altitude by factors of 15 and 4, respectively.

Finally, there is no evidence of variations in $^{13}\text{C}/^{12}\text{C}$ or D/H (Nixon et al. 2012; Molter et al. 2016, respectively) with latitudes or seasons, and the analysis of De Kok et al. (2007) from Cassini/CIRS observations in the stratosphere over a latitudinal range of 75°S to 35°N argues for a latitudinally uniform CO profile, consistent with Gurwell (2004), Gurwell & Muhleman (2000), Maltagliati et al. (2015a), and Rannou et al. (2022), which is expected given its very long ascent time in the Titan’s stratosphere.

As shown in Figure 2, the highest relative differences in I/F are confined in specific wavelength ranges and are systematically lower than 3% in the methane bands and lower than 0.7% in the atmospheric transmission windows. As all the gas in the model are radiatively active, the main driver of the changes in simulated spectra is the T - P profile. Modifying the methane VMR changes by less than 1% the simulated I/F in the cores of the methane bands and by less than 0.5% in the atmospheric transmission windows, weakly affecting the integrated column opacity. Changing the HCN and C_2H_2 VMR has an effect only at their absorption band near $3 \mu\text{m}$, which is a wavelength region that we do not use in our inversions (see Appendix B). In conclusion, keeping the temperature and gas VMR profiles fixed in the model with their recommended values (Table 1, middle column) results in extremely weak biases, almost indiscernible in the atmospheric

transmission windows. As a consequence, this only weakly affects the estimation of the aerosol opacity, and thus of the surface albedo, as shown in Section 3.2.

2.2.2. Gas Line Lists and Absorption Coefficients

Molecular absorption in the atmosphere is treated thanks to the ad hoc computation of precomputed correlated- k coefficients for $^{12}\text{CH}_4$, CH_3D , $^{13}\text{CH}_4$, CO , C_2H_2 , and HCN , as this method is less time-consuming than line-by-line calculation. The coefficients, which come from Coutelier et al. (2021), are calculated separately once on the reference pressure grid from Fulchignoni et al. (2005), interpolated to the pressure levels corresponding to the radiative transfer model grid for each wavelength, taking into account the progressive VIMS wavelength shift—from 0 to 15 nm—reported from the beginning to the end of the mission (Clark et al. 2018). A four-point Gaussian quadrature is used to integrate the cumulative k distribution and produce the set of correlated- k coefficients. Methane and its isotopes opacities are simulated as described in Rey et al. (2018) using recent developments from laboratory measurements ($T = 50$ – 350 K). This is the first accurate unified theoretical methane line lists of $^{12}\text{CH}_4$ and $^{13}\text{CH}_4$ up to $13,400 \text{ cm}^{-1}$ ($> 0.75 \mu\text{m}$). CO , C_2H_2 , and HCN correlated- k coefficients are calculated from the HITRAN database (Rothman et al. 2013). For the line broadening, the line profiles are represented by a Voigt function with collision broadening coefficients from Menard-Bourcin et al. (2007), and a cutoff for the Lorentzian far wings is set at 26 cm^{-1} from the line center for all lines and modified with a sub-Lorentzian exponential decay with a wavenumber characteristic length of 120 cm^{-1} for all species except CO (Campargue et al. 2012). For the latter, we used the recommended cutoff by Lellouch et al. (2003). Despite recent improvements in the spectroscopic databases, the line lists of numerous species, including ethane, which may have important contributions in the 2.0–2.7 and 3.0–3.7 μm ranges (Maltagliati et al. 2015a), are still not available.

2.2.3. Haze Aerosols Model

Tomasko et al. (2008) and Doose et al. (2016) recommended the use of phase functions, single-scattering albedos, and extinction profiles that best fit the DISR measurements, based on an idealized aerosol structure, i.e., fractal aggregates of 3000 spherical monomers 50 nm in radius and fractal dimension 2. The mean radius of the monomers was constrained by the high degree of linear polarization measured by DISR. Monomer radii must be less than about $0.05 \mu\text{m}$ to give sufficient polarization in a single scattering to produce the degree of

linear polarization measured in Titan’s atmosphere at 140 km altitude (Tomasko et al. 2008). This measure is relatively independent of the fractal dimension since polarimetric data around 90° phase angle are mainly sensitive to the radius of the monomers and not to the fractal dimension (Rannou et al. 1997). The number of monomers was constrained by the width of the forward-scattering peak. Isophote contours of the solar aureole, as measured by DISR during the Huygens descent, are best fitted by a model with 3000 monomers of radius 0.05 μm and an optical depth profile that agrees with the constraints of the visible spectrometer systems (Tomasko et al. 2008), again regardless of the fractal dimension.

In the work of Tomasko et al. (2008) and Doose et al. (2016), solely the fractal dimension is not constrained by observations and is set to 2. This fractal dimension corresponds to the theoretical value associated with the ballistic cluster-cluster aggregation mode that is assumed to prevail in the stratosphere for Titan’s aerosol growth (Meakin 1984; Cabane et al. 1992, 1993). The fractal aggregate model of Tomasko et al. (2008), and later on of Doose et al. (2016), successful in reproducing with a high degree of accuracy the wealth of in situ Huygens observations, was intensively used as the canonical model of Titan’s haze aerosols for a decade (e.g., Rannou et al. 2010; Griffith et al. 2012; Hirtzig et al. 2013; Solomonidou et al. 2014, 2016, 2018, 2020; Brossier et al. 2018; Rodriguez et al. 2018). Numerous studies, some including microphysical modeling (e.g., Lavvas et al. 2011; Coutelier et al. 2021; Rannou et al. 2022), showed that the fractal dimension of haze aerosols could exceed 2 and even reach 2.3–2.4. We thus redefine our aerosol model by replacing the use of tabulated values coming from the modeling of Tomasko et al. (2008) and Doose et al. (2016) with a more flexible approach allowing for self-consistent calculations of the optical properties of fractal aggregates. To do so, we coupled our RT model with a fractal aggregate scattering model, following the work of Coutelier et al. (2021). This aerosol model consists of a model that calculates the absorption and the scattering of aggregates of identical spheres assuming a fractal structure of the aggregate and a resolution method that relies on a “mean field” approximation (Botet et al. 1997; Rannou et al. 1997). This model allows for the computation of the fractal aggregate optical properties, i.e., single-scattering phase functions, single-scattering albedos, and absorption and scattering cross-sections, given the number and size of monomers, the fractal dimension, and the monomer refractive indices. Here, we use refractive indices that are an updated version of those of Titan’s aerosol laboratory analogues measured by Khare et al. (1984), modified with the help of Cassini VIMS and CIRS observations in the 100–500 km altitude range (Rannou et al. 2010; Vinatier et al. 2012). Given that the number and size of monomers are robustly constrained, independently of the fractal dimension, only fractal dimension is a free parameter of the fractal aggregate model.

Following in situ Huygens observations (Tomasko et al. 2008; Doose et al. 2016) and recent analyses of Cassini/VIMS observations by Coutelier et al. (2021), we also distinguish two main aerosol populations: (1) a photochemical haze layer composed of fractal aggregates above 55 km, and (2) a mist layer below. As it is subject to the tropopause’s low temperature, and thus condensation of organic species (Hanel et al. 1981; Yung et al. 1984), the moniker “mist” is used to

describe an undefined mixture of the above photochemical haze and condensed material.

All this considered, we can calculate from the fractal aggregate scattering model the aerosol optical properties needed as inputs for our RT modeling: extinction profile, single-scattering albedo, and phase function, as a function of altitude and VIMS wavelength.

Following Coutelier et al. (2021), we compute the haze and mist extinctions by modifying the haze and mist optical depth vertical profiles of Doose et al. (2016) as follows:

$$\begin{cases} \tau_{h,D_f}(z, \lambda) = F_h \tau_h(z, \lambda_0) \frac{\sigma_{\text{ext},D_f}(\lambda)}{\sigma_{\text{ext},D_f}(\lambda_0)} & \text{for } z \geq 55 \text{ km} \\ \tau_{m,D_f}(z, \lambda) = F_m \tau_m(z, \lambda_0) \frac{\sigma_{\text{ext},D_f}(\lambda)}{\sigma_{\text{ext},D_f}(\lambda_0)} & \text{for } z < 55 \text{ km} \end{cases}, \quad (1)$$

with σ_{ext,D_f} the extinction cross section computed with the fractal aggregate model for a fractal dimension D_f , and τ_h and τ_m the haze and mist optical depths taken from Doose et al. (2016). The extinction profiles of the haze and mist are normalized at an arbitrary reference wavelength λ_0 , here 1 μm . These profiles are adjustable thanks to two scaling parameters: F_h for the haze and F_m for the mist.

The haze single-scattering albedo $\omega_0(\lambda)$ is consistently computed by the fractal aggregate model for a given fractal dimension D_f . We include in our RT model the transition observed by Huygens during the descent as reported in Doose et al. (2016): Above 200 km, $\omega_0(\lambda)$ is computed with the fractal aggregate model, below 80 km, $\omega_0(\lambda)$ is defined as $\omega(\lambda, z < 80 \text{ km}) = (0.565 + \omega(\lambda, z > 200 \text{ km}))/1.5$, and between these two altitudes, $\omega_0(\lambda)$ is linearly interpolated.

Haze and mist phase functions are also calculated with the fractal aggregate scattering model for the fractal dimension D_f . Following the recommendation of De Bergh et al. (2012) and Doose et al. (2016), our starting hypothesis is that the same phase functions should be used for the haze and the mist. Nevertheless, the analysis of multiangular observations of Titan by VIMS recently showed that corrective factors should be applied to the backscattering region of the phase functions, independently of the haze and the mist (S. Rodriguez et al. 2023, in preparation). During the 88th flyby of Titan, VIMS acquired over 5 minutes a series of 26 cubes pointing over the same area. This sequence, equivalent to an emission phase function (EPF), thus constitutes 26 observations spanning a range of emission and phase angles of 47°–63° and 0°–70° respectively, offering a unique opportunity to probe the angular properties of Titan’s aerosols and surface in the backscattering domain. Investigating haze and mist phase curves thanks to the T88 EPF sequence, we found that haze and mist phase functions provided by the fractal aggregate scattering model with the recommended fractal dimension 2.4 must be further corrected by using multiplicative factors of 1.4 for the haze and 2 for the mist in the 0°–70° phase angle domain, at all wavelengths (S. Rodriguez et al. 2023, in preparation). The corrected phase functions are reported in Figure 3(d). We apply these haze and mist phase function corrections in our RT-IPGP-2022 model.

2.3. Summary of Differences between RT-IPGP-2016 and RT-IPGP-2022

All the updates regarding the atmospheric parameters (temperature profile, gases VMR, and gaseous and aerosol optical properties) of the RT-IPGP-2022 model with respect to

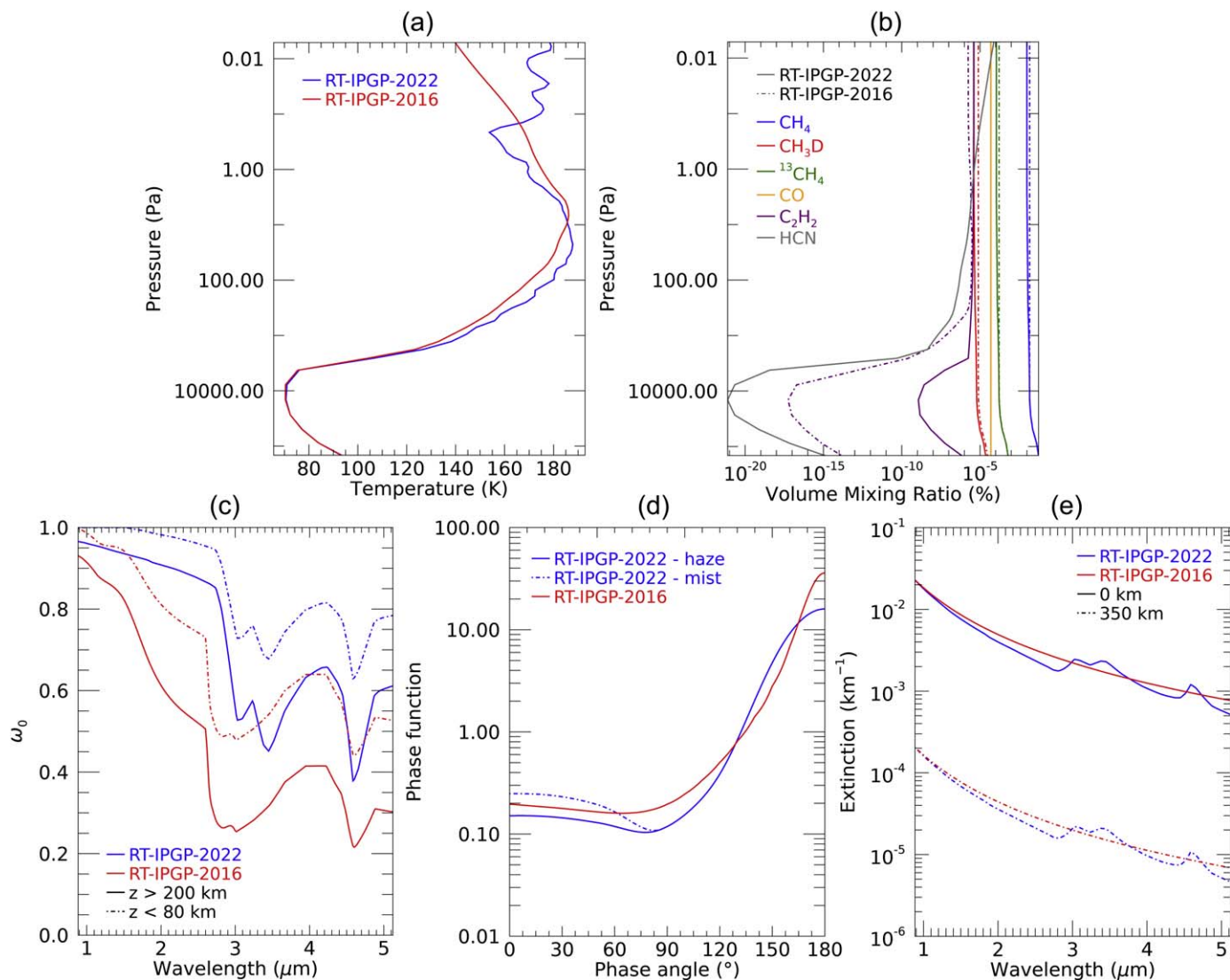


Figure 3. Comparison between RT-IPGP-2016 and RT-IPGP-2022 input parameters. (a) Pressure–temperature profiles, (b) gas volume mixing ratio profiles, (c) aerosol single-scattering albedos for two altitude regimes, (d) aerosol single-scattering phase functions at $2.53 \mu\text{m}$, and (e) aerosol extinction profiles.

the previous version (RT-IPGP-2016) are summarized in Table 1 and illustrated in Figure 3.

We simulate a Titan’s spectrum using both the RT-IPGP-2016 and RT-IPGP-2022 models under the same configuration (i.e., observation angles to 0° , surface albedo set to 0, and aerosol scaling factors set to 1 relative to the aerosol opacity observed by Doose et al. 2016). We then switch on one by one all the input parameters of the RT-IPGP-2022 model to replace those used in the RT-IPGP-2016 model and calculate the residuals between these spectra due to a given parameter. All the results of these analyses are shown in Figure 4.

The simulated spectra show that the major difference between RT-IPGP-2016 and RT-IPGP-2022 models comes from the background spectral slope. The spectra indeed cross at $\lambda \approx 2 \mu\text{m}$ due to the difference in the spectral dependency of the aerosol opacity between models (Figure 3(a)). This is best illustrated by the residuals between the 2016 and 2022 models (Figures 3(b) and (e)), where we show that the change in aerosol optical properties contributes the most, with maxima in regions of low atmospheric opacity, especially at the shortest wavelengths, below $2 \mu\text{m}$. Here, the change in aerosol phase functions has the highest impact on simulated spectra. Updates

in the temperature–pressure profile, gas line lists, and VMR (Figures 3(b)–(d)) have a much lower contribution—one order of magnitude lower—with, as expected for the gases, maxima in wavelength regions of high opacity.

All the differences between the 2016 and 2022 models have consequences for the aerosol opacity and surface albedo retrievals. This will be explored in depth and validated with the help of the available in situ Huygens measurements in the following section.

3. Inversion of Orbital Observations of the Huygens Landing Site with the RT-IPGP-2022 Model and Validation with Huygens Observations

3.1. Cassini/VIMS Observations of the Huygens Landing Site

3.1.1. Cassini/VIMS

VIMS was an imaging spectrometer part of the payload of the Cassini spacecraft. VIMS performed observations within 96 channels in the visible from 0.3 to $1 \mu\text{m}$, with a mean spectral sampling capability of 7.3 nm , and within 256 channels in the infrared (IR) from 0.884 to $5.110 \mu\text{m}$, with a mean spectral

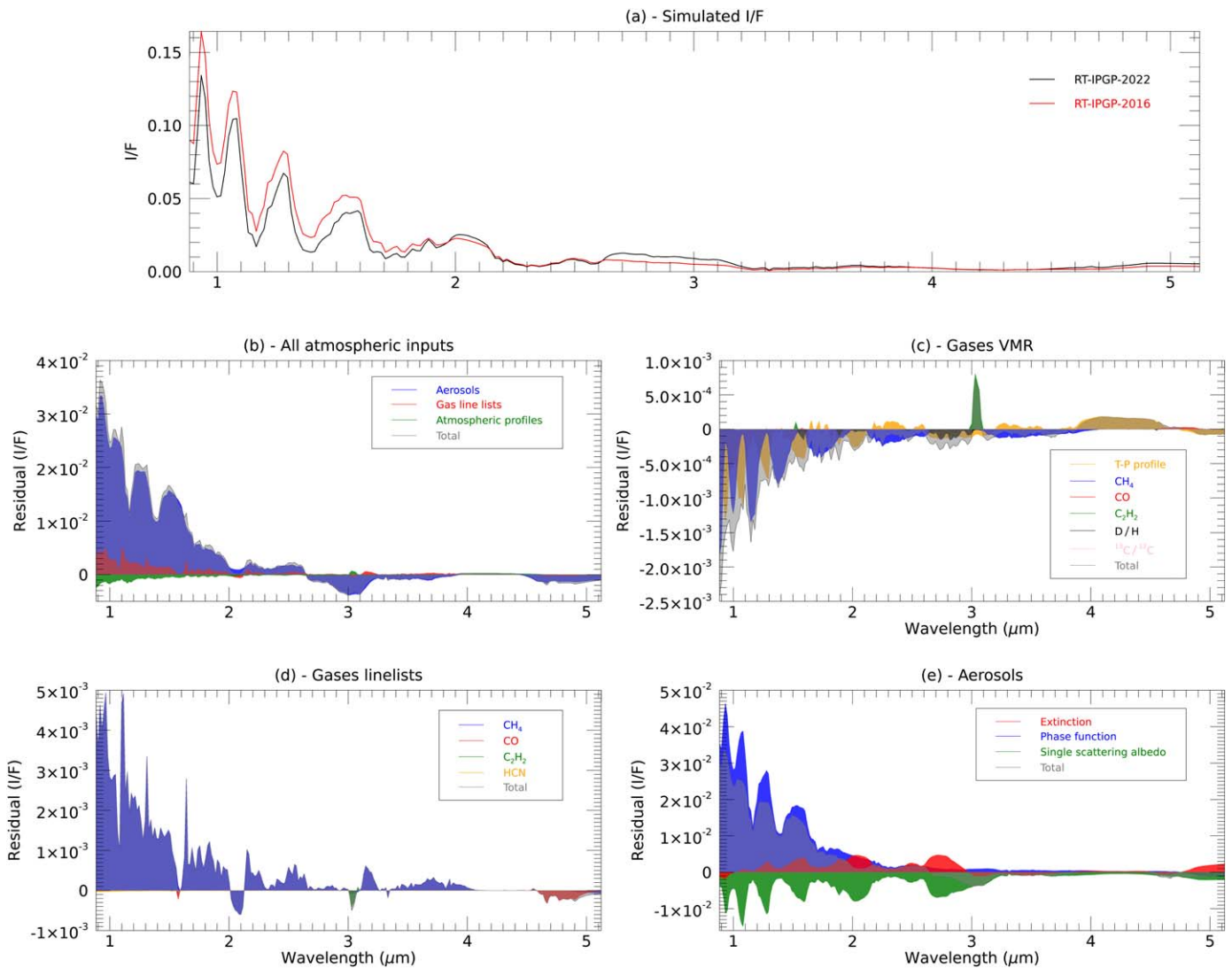


Figure 4. (a) I/F spectra simulated by the RT-IPGP-2016 (red line) and RT-IPGP-2022 (black line) models under the same configuration (i.e., incidence, emission, phase angles set to 0° , surface albedo set to 0, and haze and mist scaling factors set to 1 with respect to the aerosol opacity observed by Huygens (Doose et al. 2016)). Bottom panels: residuals between RT-IPGP-2016 and RT-IPGP-2022 simulations due to (b) all atmospheric inputs, (c) gas VMR only, (d) gas line lists only, and (e) aerosols only.

sampling capability of 16.6 nm. In this work, we only deal with the infrared part of the spectrum. We perform the radiometric calibration of the raw data into I/F as a function of wavelength for each of the 256 VIMS-IR channels using the standard RC19 VIMS pipeline (Clark et al. 2018). This calibration includes a time-dependent radiometric calibration aimed at correcting a wavelength shift that has been identified during the last years of the mission (Clark et al. 2018). Up to ≈ 15 nm of progressive shift is observed when comparing data taken in 2004 and data taken in 2017. This shift can dramatically alter the surface information in the sharp atmospheric windows (especially the narrow ones at short wavelengths) because of the wide-band correlated- k coefficients calculation used in our RT model. For every pixel, we determined the viewing geometry and location information using the SPICE (Spacecraft, Planet, Instrument C-matrix—“Camera matrix”—Events) toolkit from NAIF (Navigation and Ancillary Information Facility) (Acton et al. 2018). Radiometric error is computed for every VIMS spectel using the scheme described in Appendix A.

3.1.2. VIMS Observation of the Huygens Landing Area

We focus on the VIMS hyperspectral cube CM_1481624349_1 acquired during flyby TB, which occurred on 2004 December 13 over the region of the Huygens landing site (HLS, $10^\circ 57'3''S$ and $167^\circ 66'5''E$; Kazeminejad et al. 2011). The cube is available on the Cassini VIMS Data Portal (Le Mouélic et al. 2019). VIMS has observed the HLS on several occasions, but we chose the observation that took place the closest in time to Huygens’ descent and landing. The short (one month) time interval between VIMS and Huygens observations, corresponding to two of Titan’s days, minimizes the chances of atmospheric and surface changes, allowing for a direct comparison between orbital and in situ observations. The 24×12 pixels² VIMS cube has a mean spatial sampling of 16×8 km² per pixel. The incidence, emergence, and phase angles of the VIMS observation vary between $31^\circ 9'$ and $38^\circ 0'$, $30^\circ 4'$ and $36^\circ 5'$, and $18^\circ 4'$ and $18^\circ 8'$, respectively. These observation angles allow us to use the plane-parallel approximation in our radiative transfer calculation.

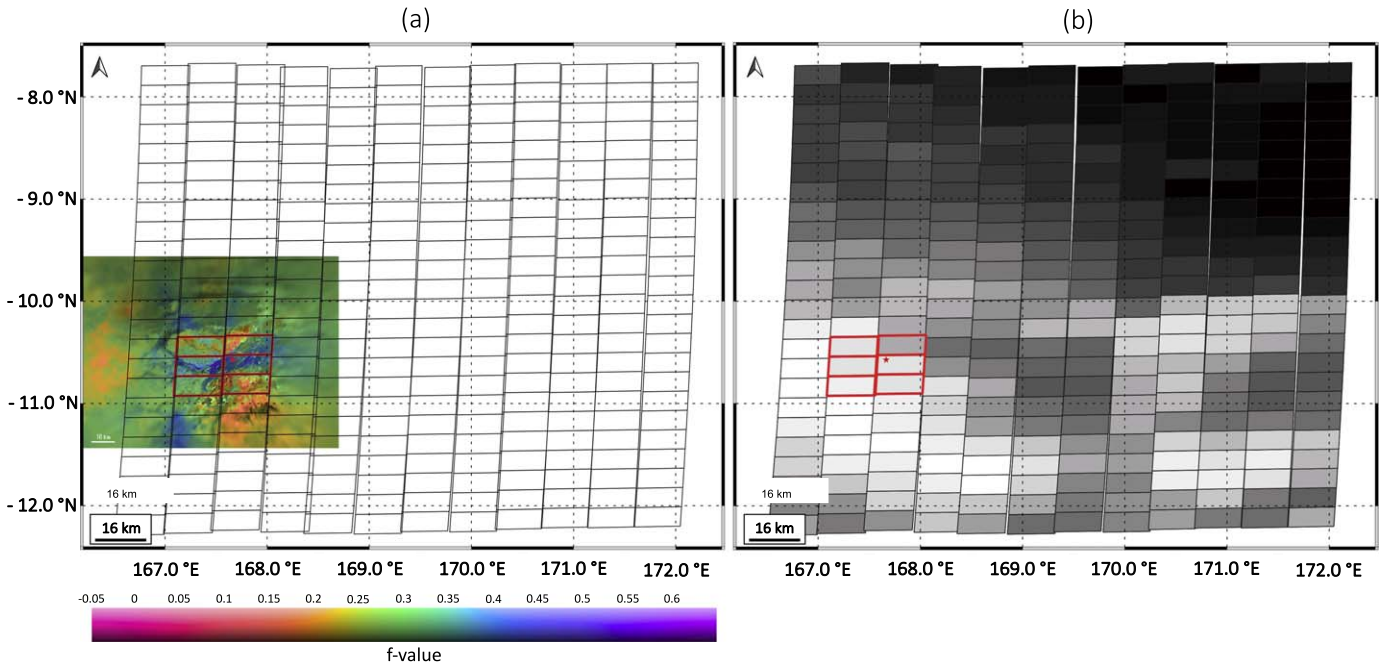


Figure 5. (a) Pixel footprints of the VIMS CM_1481624349_1 cube superimposed on the color-coded photometrically calibrated mosaic of Karkoschka & Schröder (2016) and the f -values/color correspondence, and (b) I/F of the VIMS CM_1481624349_1 cube at 2.018 μm . Pixels used for the endmember extraction are highlighted in red.

3.1.3. Extraction of the Spectrum of the Huygens Landing Site from the VIMS Cube

We use the VIMS CM_1481624349_1 observation over the HLS to validate our RT-IPGP-2022 model by comparing it with the in situ Huygens/DISR spectral measurements. First, we extract the most representative spectrum of the HLS from the VIMS data cube. To do so we superimpose the CM_1481624349_1 data cube over the highest-resolution mosaic. We use the photometrically calibrated mosaic of Karkoschka & Schröder (2016) constituted of about 300 images taken by the Huygens/DISR instrument starting from 70 km altitude at 770 nm wavelength (Karkoschka et al. 2007, and refined by Karkoschka et al. 2012). Since the spatial resolution of the VIMS data cube does not allow us to distinguish as many small-scale surface features at the landing site, many attempts have been done to reconstruct the HLS spectrum with linear combinations of VIMS pixels around the HLS (e.g., Griffith et al. 2012; Hirtzig et al. 2013; Corlies et al. 2021). But the method, the choice of VIMS pixels, and the calculation of the linear combination coefficients were not explicitly described and our tests with these different combinations showed that they were not accurate enough for a valid comparison. The DISR mosaic reveals the presence of different brightness units in the surroundings of the HLS, with a spatial resolution of about 1% of the distance to the HLS (i.e., 1 km at 100 km from the HLS and 50 cm at 50 m from the HLS). Over the same region covered by the DISR albedo mosaic, Karkoschka & Schröder (2016) built a map of the photometric parameter f , standing in for the relative contribution of isotropic (Lambert) to anisotropic (Lommel–Seeliger) surface scattering. The f -parameter map showed that, beyond albedo differences, this region can be characterized by units of variable photometric behavior (a proxy for surface composition and/or texture differences) at spatial resolutions below those accessible to VIMS, as shown in Figure 5. The color code of

the map, displayed in Figure 5(a), stands for the f -values. Purple, blue, green, orange, and pink colors correspond to the highest (0.65), high (0.5), medium (0.3), low (0.2), and lowest (−0.05) f -values, respectively (Karkoschka & Schröder 2016).

If we assume that, in the transmission windows, the VIMS spectrum of a given pixel is a linear combination of the spectra of surface spectral units, or endmembers, weighted by their respective fractional coverage within the pixel, we can write

$$V = \sum_{n=1}^N E_n \alpha_n, \quad (2)$$

with V the observation spectrum, N the number of endmembers, E_n the spectrum of the endmember n , and α_n the fractional coverage of the endmember n in the observation. Two physical constraints are imposed for consistency reasons, as $\alpha_n > 0$, $\forall n$ to avoid unphysical negative abundances, and $\sum_{n=1}^N \alpha_n = 1$. Spectral mixture analyses have been performed on hyperspectral image data for several solid planetary bodies in the solar system, such as the Moon (Li & Mustard 2003), Mars (Combe et al. 2008), asteroids (Combe et al. 2015), and Titan (McCord et al. 2008). The VIMS pixel over the HLS being the result of a linear mixture of photometric units, we apply linear unmixing to a selection of VIMS pixels close to the HLS with the help of the higher-resolution f -parameter map in order to extract the VIMS spectrum that best corresponds to the photometric unit (i.e., the best combination of both composition and texture) of the HLS itself. First, the f -parameter map was segmented into photometric parameter clusters/endmembers using a k -means clustering algorithm. Six pixels of the CM_1481624349_1 VIMS cube neighboring and including HLS (i.e., pixels [8,2], [9,2], [10,2], [8,3], [9,3], [10,3]) were geographically projected and superimposed onto

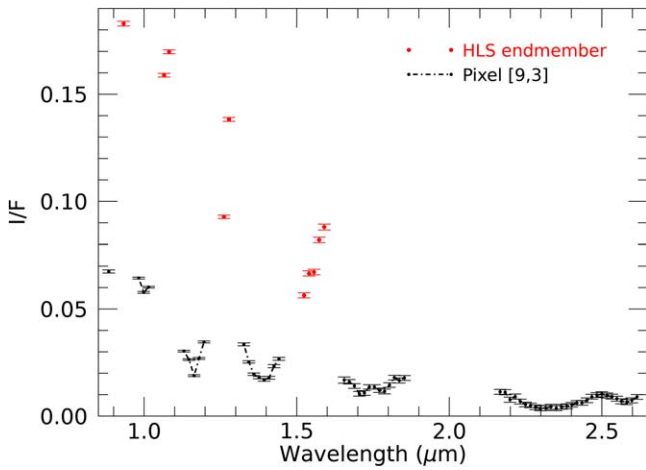


Figure 6. HLS endmember spectrum from 0.88 to 2.6 μm computed from the VIMS cube CM_1481624349_1. In the methane bands (black dots), I/F values come from the pixel including the HLS (pixel [9,3]). In the atmospheric windows (red dots), I/F values are reconstructed by recombining neighboring pixels in order to best represent the spectrum of the HLS spectral/photometric unit. 2σ radiometric error bars are shown in black and 2σ propagated radiometric error bars are shown in red.

the f -parameter map to measure for each pixel the surface fraction covered by each of the photometric endmember previously identified. A combination of linear equations (as many as the VIMS pixels; see Equation (2)), allows for the retrieval of a spectrum that best represents the spectral/photometric endmember of the HLS using a matrix inversion routine. The equation of the linear combination of each VIMS pixel spectrum used to reconstruct the HLS endmember is given in Equation (3):

$$E = \begin{pmatrix} 0.125 \\ 0.658 \\ 0.005 \\ 0.006 \\ 0.598 \\ 0.314 \end{pmatrix} * \begin{pmatrix} [8, 2] \\ [9, 2] \\ [10, 2] \\ [8, 3] \\ [9, 3] \\ [10, 3] \end{pmatrix}. \quad (3)$$

The uncertainties on the HLS endmember spectrum are calculated by propagating the radiometric errors on the VIMS spectra used in the combination. We tested different numbers of endmembers for the segmentation of the f -parameter mosaic. We found that beyond five endmembers, the resulting HLS endmember spectrum does not present any variations greater than the spectrum error bars. This spectrum is computed only in the atmospheric transmission windows and, considering that Titan’s atmosphere presents uniform properties at the VIMS observation pixel scale, the HLS endmember spectrum is completed in the methane bands by the values of I/F from the VIMS pixel including the HLS. We show in Figure 6 the reconstructed HLS endmember spectrum. Since the DISR wavelength range stops at 1.6 μm , we choose to compute the HLS endmember in the windows only up to this wavelength.

3.2. Aerosol Vertical Distributions Retrieval from the VIMS HLS Spectrum

The HLS endmember spectrum derived from the VIMS cube CM_1481624349_1 is used to extract the haze and mist vertical

distributions over the site of Huygens entry, descent, and landing, to be further compared with in situ DISR measurements.

We compute the I/F in the atmospheric bands (using only the “haze/mist spectel”—see Appendix B) with the help of our RT-IPGP-2022 model for various haze and mist scaling factors F_h and F_m , and for different aerosol fractal dimensions. We use the MPFIT algorithm (Markwardt 2009), which performs a nonlinear least-squares Levenberg–Marquardt fit based on a gradient descent in order to maximize the goodness of fit between the simulated spectra and the HLS endmember spectrum. The goodness of fit is estimated by the classical reduced- χ^2 function of merit,

$$\chi_{\text{red}}^2 = \frac{1}{\nu} \sum_{i=1}^N \left(\frac{(I/F)_i^{\text{obs}} - (I/F)_i^{\text{sim}}}{\sigma_i} \right)^2 \quad (4)$$

with i the VIMS spectral number, $(I/F)_i^{\text{obs}}$ the I/F of the HLS endmember spectrum, $(I/F)_i^{\text{sim}}$ the I/F computed with the RT model, σ the 1σ radiometric error of the HLS endmember spectrum, and $\nu = n - m$ the degrees of freedom, i.e., the number of observations $n = 58$ (number of VIMS spectels used for the inversion) minus the number of free parameters $m = 2$. The inversion of the haze and mist populations (F_h and F_m) from the HLS endmember spectrum requires roughly 30 minutes of computation time. This is performed for seven values of aerosol fractal dimensions, from 2.0 to 2.6 by 0.1 increment. At the convergence of the inversion process, the MPFIT algorithm gives direct access to the free parameters F_h and F_m and their 1σ uncertainties.

We present in Table 2 the χ_{red}^2 , F_h and F_m values, and their 2σ uncertainties corresponding to the best fits for each aerosol fractal dimension that we have tested. Consistent with Coutelier et al. (2021) and Rannou et al. (2022), we found that $D_f = 2.3\text{--}2.4$ give the best fit ($\chi_{\text{red}}^2 = 8.22\text{--}8.20$) to the HLS observations, using tholin’s refractive indices from Khare et al. (1984) modified by Rannou et al. (2010), confirming the need for a reassessment for Titan’s aerosol fractal dimension. We show in Figure 7 and in Figure 8 the best fits for the different fractal dimensions and the RT-IPGP-2016 model for comparison. The best fit using the RT-IPGP-2016 model gives a $\chi_{\text{red}}^2 = 15.91$, almost two times higher than the best fit with the RT-IPGP-2022, which better simulates the spectral behavior of the aerosols with an aerosol fractal dimension of 2.3–2.4.

Once the haze and mist populations have been evaluated, we can extract the surface albedo of the HLS in the atmospheric windows from the HLS endmember spectrum (using the “surface spectels”—see Appendix B). This procedure will be detailed in Section 3.3.2.

We finally present here the result of the sensitivity study on the fixed input parameters (see Section 2.2.1) on the F_h and F_m parameters retrieved from the HLS endmember spectrum for the best-fit case ($D_f = 2.4$). When modifying all the fixed input parameters listed in Section 2.2.1 to their extreme possible values, the retrieved aerosol opacity scaling factors, with 2σ uncertainties, are $F_h = 1.1 \pm 0.1$ and $F_m = 1.1 \pm 0.2$, for a χ_{red}^2 of 7.8. These values are included in the error bars of the F_h and F_m parameters retrieved with the recommended set of atmospheric parameters (see Table 1, middle column). The simulated spectra with these different atmospheric profiles are therefore indistinguishable and the

Table 2
Best-fitting χ_{red}^2 , as Well as F_h and F_m with 2σ Uncertainties as a Function of the Aerosol Fractal Dimension D_f

D_f	2.0	2.1	2.2	2.3	2.4	2.5	2.6
χ_{red}^2	16.6	15.2	11.3	8.2	8.2	13.2	26.7
$F_h^{\pm 2\sigma}$	$1.3^{\pm 0.1}$	$1.2^{\pm 0.1}$	$1.1^{\pm 0.1}$	$1.1^{\pm 0.1}$	$1.0^{\pm 0.1}$	$1.0^{\pm 0.1}$	$1.0^{\pm 0.1}$
$F_m^{\pm 2\sigma}$	$0.9^{\pm 0.3}$	$0.8^{\pm 0.3}$	$1.0^{\pm 0.3}$	$1.1^{\pm 0.2}$	$1.2^{\pm 0.2}$	$1.4^{\pm 0.2}$	$1.6^{\pm 0.3}$

modification of those atmospheric input parameters within their expected variation range has no impact on the values of the inversion outputs (F_h and F_m parameters and by extension the surface albedo). This is totally consistent with the analysis of Rannou et al. (2022).

3.3. Validation of the RT-IPGP-2022 Model with Atmospheric and Surface Huygens Measurements

3.3.1. RT-IPGP-2022 Atmospheric Model Validation with Huygens/ DISR-ULIS

Here we compare the spectra acquired by the Huygens/ DISR Upward Looking Infrared Spectrometer (ULIS) instrument during the probe's descent into Titan's atmosphere with synthetic spectra simulated with our RT-IPGP-2022 model. The simulated spectra are directly calculated with the haze and mist opacities previously retrieved from the HLS endmember spectrum for aerosol $D_f = 2.4$ (see Section 3.2) and the surface albedo measured by DISR (Karkoschka et al. 2012).

The ULIS instrument covers a spectral range of 830–1620 nm and recorded spectra from an altitude of 141 km down to the surface and after landing (Tomasko et al. 2008). ULIS is made of a linear array of 150 detector elements. A horizontal diffusing plate and an optical deflector limited its total field of view (FOV) to 170° in azimuth and from 5° to 88° in zenith angle. The data collection was managed by the DISR solar sensor system and, due to the unexpected rotation direction of the probe, data were acquired by integrating over random azimuth angles relative to the Sun rather than at well-defined azimuths as planned. A total of 214 spectra were acquired by ULIS: 4 spectra per 48 observation sequences from 141 to 5.3 km, plus 22 observations made in snapshot mode (short exposure time) from 3 km down to the surface. ULIS spectra, calibrated in radiance ($\text{W m}^{-2} \mu\text{m}^{-1} \text{sr}^{-1}$), are archived in the ESA Planetary Science Archive and in the NASA Planetary Data System (PDS), along with information relevant to each of the observation sequences (altitude, solar zenith angle, and Huygens rotation speed and tilt).

At the nodes of our RT model altitude grid, we can only extract, over the ULIS wavelength range, up- or down-welling hemispheric integrated fluxes radioed to the incoming solar flux. We therefore had to convert ULIS radiances into I/F to be consistent with the outputs of our RT model.

To do so, we had first to correct each observation for the rotation of the probe during the acquisition time, the nonuniform data distribution in azimuth, the nonhomogeneous response of the ULIS FOV in solar zenith angle, and the probe's tilt. This is done by dividing each ULIS radiance

spectrum by a global corrective factor F , defined as follows:

$$F = \frac{f}{f_{\text{corr}}}(1 + 0.042 T). \quad (5)$$

The solar factor f , defined in Tomasko et al. (2008) and Bézard (2014), represents the direct solar flux contribution in the ULIS FOV averaged over the azimuth angles of the integration sequence and normalized such that $f = 0$ if the Sun is never in the FOV and $f = 1$ if the spectrum is collected with a uniform distribution in azimuth from 0° to 360° . f is calculated for each individual ULIS spectrum using the calibration information for the DISR infrared instruments.¹³ To account for the nonideal spatial response of the instrument with respect to the solar zenith angle, the solar factor f is further divided by a corrective factor f_{corr} defined as

$$f_{\text{corr}} = \mu_s \frac{2 \int_0^1 R(\mu) d\mu}{R(\mu_s)}, \quad (6)$$

with μ_s the cosine of the solar zenith angle and $R(\mu)$ the FOV response as a function of the zenith angle. We correct for the tilt T (expressed in degrees in Equation (5)) with a simple linear function knowing that a tilt of $+10^\circ$ (a positive inclination stands for the Huygens rotation axis pointed to the east and thus the Sun pointed at a lower zenith angle for the ULIS FOV) increases the direct flux by about 42% compared to zero tilt, as estimated from the ULIS calibration document.¹⁴

However, the tilt values available in the data archive (DISR Data User's Guide; Karkoschka et al. 2007)¹⁵ should be used with caution. The Doppler shift measurements were used to constrain only the Earthward component of Huygens' velocity during 42 sections of the descent, not accounting for the other axes of oscillation of the probe, with linear interpolation between sections. Forty gaps were due to calibration requirements, while a larger gap was observed when switching from one radio telescope to another on a different continent due to Earth's rotation (Bird et al. 2005). Besides, the tilt was resampled at a lower frequency than the oscillations. In order to minimize all of these nonquantifiable uncertainties, we only

¹³ http://atmos.nmsu.edu/PDS/data/hpdisr_0001/DOCUMENT/DISR_CALIBRATION_DOCUMENTS/INFRARED_SPECTROMETERS/IR_SPECTROMETER_CAL_NOTES/IR_SPECTROMETER_CAL_NOTES.PDF

¹⁴ http://atmos.nmsu.edu/PDS/data/hpdisr_0001/DOCUMENT/DISR_CALIBRATION_DOCUMENTS/INFRARED_SPECTROMETERS/IR_SPECTROMETER_CAL_DOC/IR_SPECTROMETER_CAL_DOC.PDF

¹⁵ https://pds-atmospheres.nmsu.edu/data_and_services/atmospheres_data/Huygens/DISR_DATA_USERS_GUIDE_2.PDF

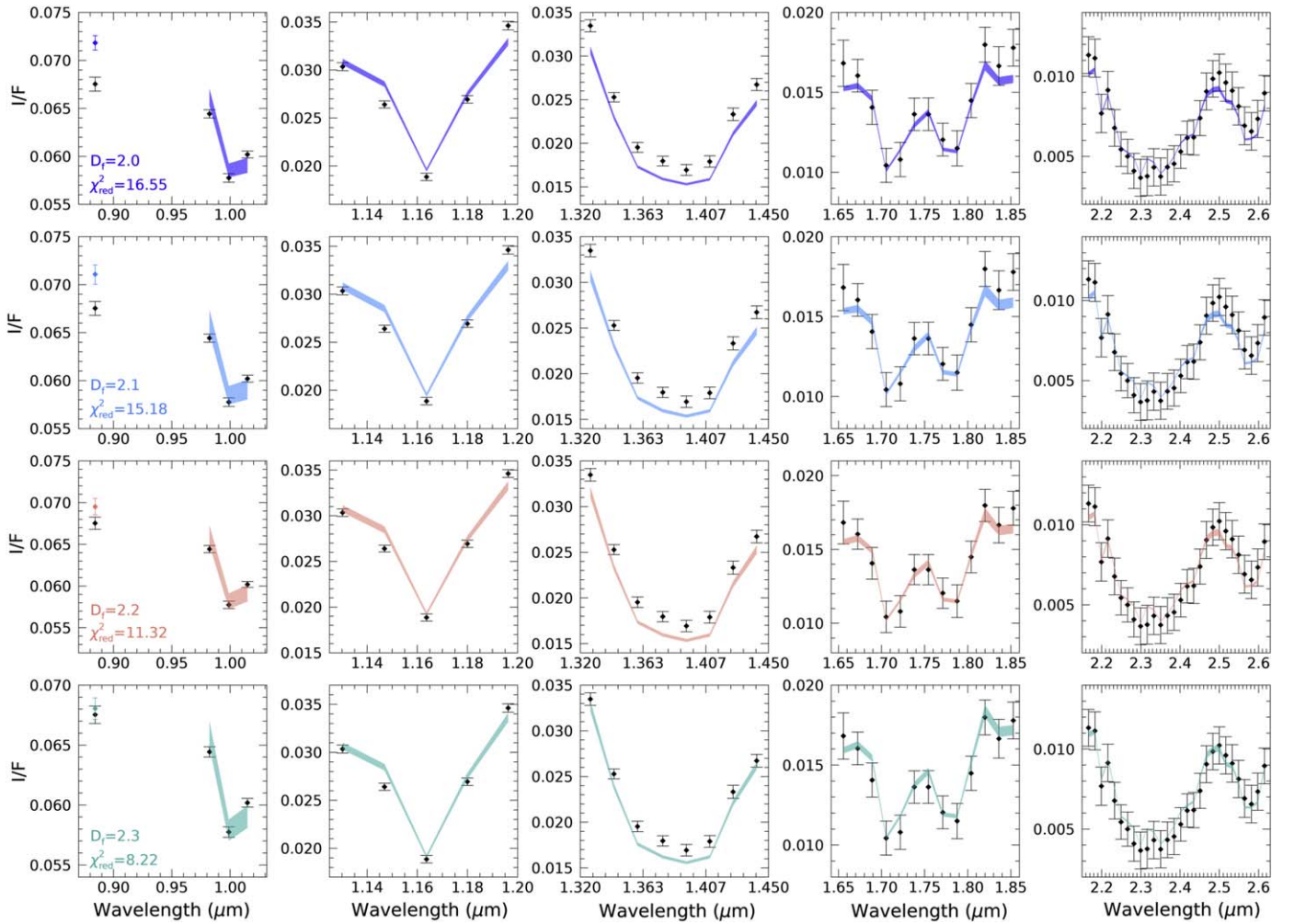


Figure 7. Fits between our model and the HLS endmember spectrum in atmospheric bands. Simulated and observed spectra are shown with their 2σ error bars. Best-fitting χ^2_{red} is given and associated F_h and F_m values with 2σ uncertainties are given in Table 2.

retained spectra for which $0.9 < F < 1.1$ and $T < 5^\circ$, reducing the number of spectra usable for our purpose from 214 to 27 and applied a linear regression at a wavelength dominated by the solar direct flux (i.e., a methane window, e.g., at $1.28 \mu\text{m}$) as a function of the altitude, as shown in Figure 9, to scale the remaining 27 observations. It is worth noting that fitting the data with a more physical function, like $a + b * e^{-z/H}$, with z the altitude and H a free parameter representative of the atmospheric scale height, does not significantly improve the fit. We averaged the spectra belonging to the same observation sequence, reducing the final number of spectra to 21.

We convert the radiances of each selected ULIS spectrum into I/F as follows:

$$\frac{I}{F}(\lambda) = I(\lambda) \pi \frac{D_{T-S}^2}{S(\lambda)}, \quad (7)$$

with D_{T-S} the Titan–Sun distance in astronomical units and $S(\lambda)$ the solar flux spectrum at 1 au (Kurucz 2005).

The resulting ULIS spectra, expressed as I/F and interpolated at our RT model (and VIMS) spectral sampling, are shown in Figure 10. The same figure also shows the spectra simulated by the RT-IPGP-2022 and the RT-IPGP-2016 models, interpolated at the altitudes of the ULIS spectra.

It is worth noting that the ULIS spectra acquired at low altitudes are the most reliable, as the diffuse solar flux, becoming dominant with respect to the direct solar flux, is significantly less sensitive to the numerous non- or only barely quantifiable uncertainties of the Huygens probe navigation (rotation speed and tilt). For the same reason, ULIS spectra are more reliable at wavelengths of the highest atmospheric opacity (i.e., in gaseous absorption bands). Also, the surface albedo seen by the probe, which was arbitrarily chosen to be equal at all altitudes to the one measured after landing, has a less and less negligible contribution to the spectra as altitude decreases. Hence, the simulated spectra are all the less trustworthy in the atmospheric windows as we are approaching Titan’s surface. We recall that synthetic spectra were simulated by our RT model using aerosol properties constrained with a spectrum extracted from a VIMS observation of the HLS. Finally, all these possible sources of uncertainties and systematic differences being considered, ULIS spectra are extremely well modeled by our RT model within wavelength (gaseous absorption bands and their wings) and altitude (below 100 km) ranges where both ULIS and simulated spectra are the most reliable. In the atmospheric bands and wings (using all spectels except the “surface spectels”—see Appendix B), the RT-IPGP-2022 model gives better matches (mean rms error

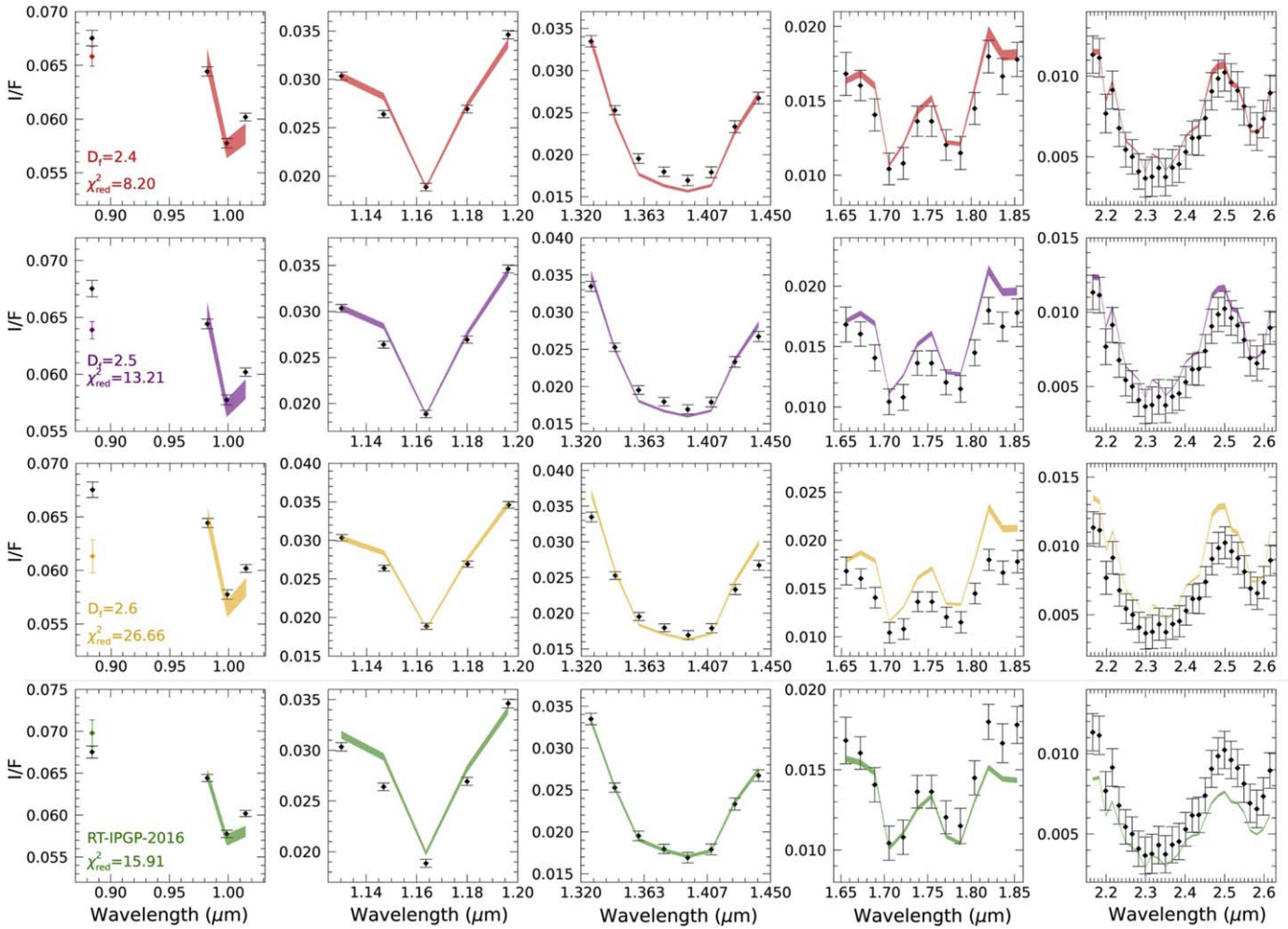


Figure 8. Fits between our model and the HLS endmember spectrum in atmospheric bands. The first three rows show the best fits for different aerosol fractal dimensions D_f and the last row for the RT-IPGP-2016 model. Simulated and observed spectra are shown with their 2σ error bars. Best-fitting χ^2_{red} is given and associated F_h and F_m values with 2σ uncertainties are given in Table 2.

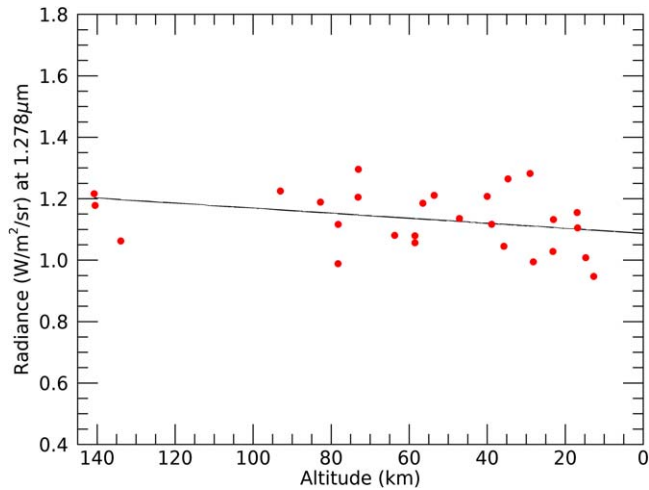


Figure 9. ULIS radiance at $1.278 \mu\text{m}$ as a function of the altitude for spectra that meet the selection criteria (red dots). The black line corresponds to the best linear fit.

over all the altitudes, or $\text{RMSE} = 0.0355$) than the RT-IPGP-2016 model ($\text{RMSE} = 0.0383$), validating our approach and the atmospheric prescriptions (for both gases and aerosols) of our RT-IPGP-2022 model.

3.3.2. Validation of RT-IPGP-2022 Surface Albedo Inversions with Huygens/DISR-DLIS

As a second step, the surface albedo is inverted in the atmospheric windows (for the “surface” spectels—see Appendix B) of the HLS endmember spectrum, using previously inverted haze and mist opacities for $D_f = 2.4$ (see Section 3.2). Our RT model computes the 2σ uncertainties on inverted surface albedos by propagating radiometric noise of the VIMS spectrum and uncertainties on the retrieved haze and mist scaling factors. I/F has been shown to be an affine law of the surface albedo in atmospheric windows with excellent accuracy. We then only need two pairs of arbitrary I/F and surface albedo correspondences per wavelength to evaluate the corresponding surface albedo, drastically decreasing the calculation time to a few seconds per spectrum. The error on the retrieved albedo amounts to at most 3% at $0.9 \mu\text{m}$ and is negligible longward of $2.1 \mu\text{m}$ (Hirtzig et al. 2013).

The surface albedos retrieved from the VIMS HLS end-member spectrum in the atmospheric windows are directly compared with the surface reflectivity measured in situ between 0.83 and $1.6 \mu\text{m}$ by the Huygens/DISR Downward Looking Infrared Spectrometer (DLIS) instrument once the probe landed. We chose for our comparison the DLIS spectrum processed by Karkoschka et al. (2012), as it is a revision of

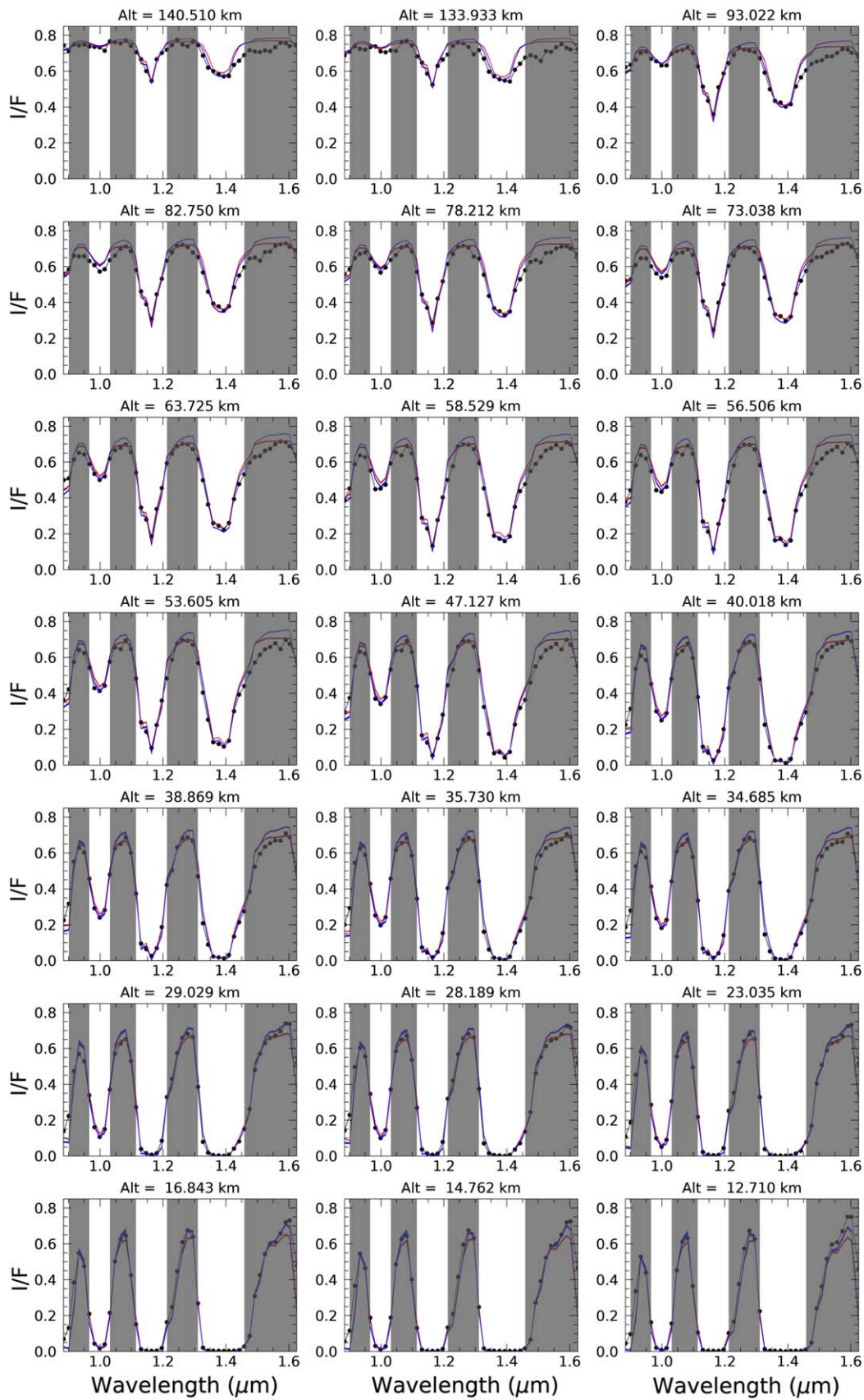


Figure 10. Comparison between ULIS (dotted black) and simulated I/F (RT-IPGP-2016 in red and RT-IPGP-2022 in blue) within the ULIS wavelength range for 21 different altitudes. Simulated spectra are coming from forward RT calculations using the haze and mist opacities estimated from the HLS endmember spectrum (see Section 3.2) and the surface albedo measured by Huygens/DISR (Karkoschka et al. 2012). The simulations are plotted along with their 2σ uncertainties envelope. Atmospheric windows are highlighted in gray.

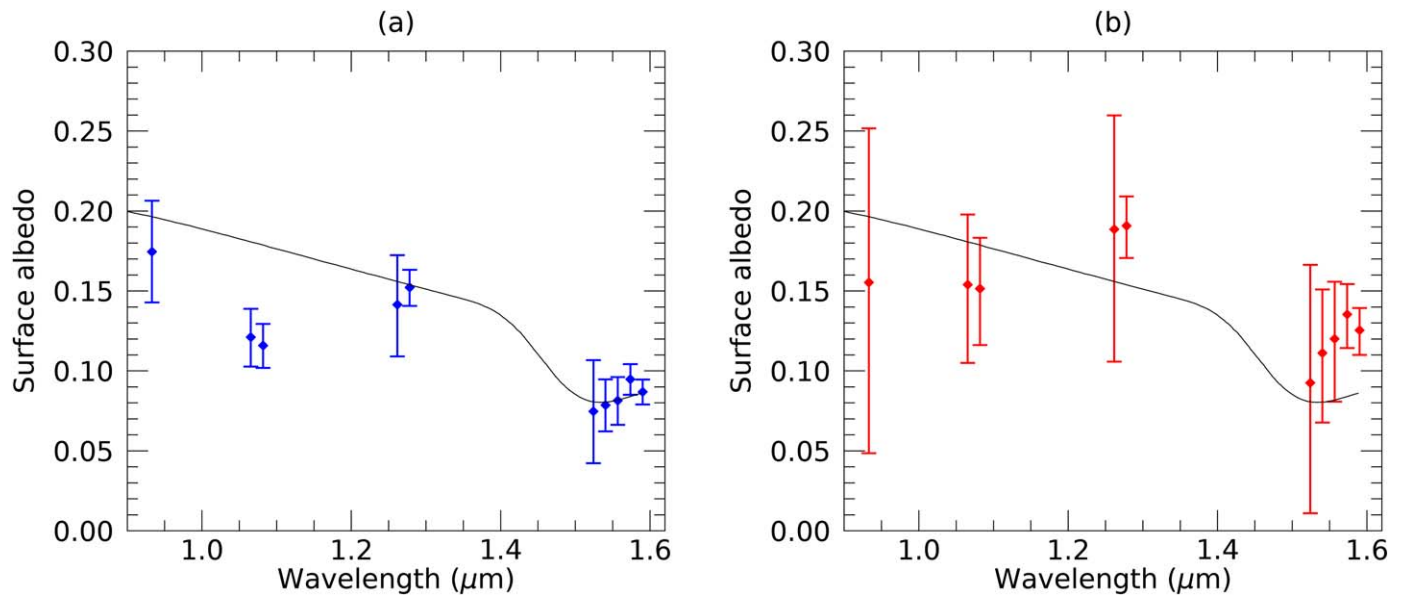


Figure 11. Surface albedos retrieved from the VIMS HLS endmember spectrum (see Section 3.1.3) in the atmospheric windows with (a) the RT-IPGP-2022 model (blue) and (b) the RT-IPGP-2016 model (red). The DLIS spectrum (Karkoschka et al. 2012) scaled by a 0.44 factor to take into account the viewing geometry is shown in black in both panels. No error bars are available for the DLIS spectrum. Inverted surface albedos are shown with 2σ error bars.

Schroder & Keller (2008) that takes into account the lamp parallax and includes a better lamp calibration and a phase angle correction. Following Rannou et al. (2016) to account for the main effects due to the observation geometry, we scaled the DLIS spectrum with a correction factor of 0.44. This factor corresponds to a factor of 0.363 between a phase angle larger than 30° and zero phase angle (Figure 8 of Karkoschka et al. 2012), divided by the cosine of the incidence angle (34° , Schröder & Keller 2009). Since atmospheric windows centered at 0.93, 1.07, and 1.28 μm are narrow, we only used one, two, and two spectels in the windows of the VIMS endmember spectrum respectively for the surface albedo inversion. Because the atmospheric window at 1.57 μm is wider, we used here five VIMS spectels.

We show in Figure 11 the retrieved surface albedos from the VIMS HLS endmember spectrum with respect to the DLIS surface reflectivity between 0.8 and 1.6 μm . The surface albedos inverted from the VIMS spectrum are shown for the RT-IPGP-2022 and RT-IPGP-2016 model configurations for the sake of comparison and validation. All the surface albedos retrieved with the RT-IPGP-2022 model present an excellent match to the DLIS spectrum within the error bars, even for the spectral slope observed in the broader 1.6 μm atmospheric window. The only exception is for the 1.07 μm atmospheric window, where our RT-IPGP-2022 fails at reproducing the DLIS reflectivity and underestimates the surface albedo by $\approx 30\%$. The same issue has already been reported by Coutelier et al. (2021) with their RT model. The origin of this problem is still under investigation and can be due to a missing opacity source from the atmosphere in our RT model (gases, haze, and/or mist) and/or a local source of surface absorption within the VIMS HLS endmember spectrum (not seen in the DLIS spectrum due to the drastic change in spatial scale, despite our effort to unmix the VIMS spectrum), in this particular wavelength range. All this considered, our RT model provides overall more robust inversions of the HLS surface albedos. For both models, summing the Euclidean distances ($D = \sqrt{\sum(S - O)^2}$) between the simulated values S and the DLIS

spectrum O over the surface spectels gives $D_{2022} = 0.091$ and $D_{2016} = 0.111$. The RT-IPGP-2022 model match with the DLIS spectrum is better than that with the RT-IPGP-2016 model and generates error bars 87.71% smaller on average on surface albedos. We conclude that RT-IPGP-2022 is a more reliable version than RT-IPGP-2016 for the retrieval of both Titan's atmosphere and surface properties.

4. Application to the Analysis of the Dragonfly Landing Area

4.1. VIMS Observations of the Dragonfly Landing Area

We now apply our RT-IPGP-2022 model with the objective of mapping the surface albedo of the Selk crater region on Titan, near the landing site of the Dragonfly mission. Dragonfly is the fourth mission in NASA's competitive New Frontiers program. Its main science objectives concern the detailed investigation of Titan's prebiotic chemistry and exotic geology (Barnes et al. 2021). The mission consists of a multi-instrumented dual-quadcopter that will arrive in Titan's equatorial region in 2033 (expected launch in 2027), in the same season as the landing of ESA's Huygens probe (Lorenz et al. 2018). The landing site, near the Selk crater ($6^\circ 5' \text{N}$, 160°E) in the Shangri-la dune field, was chosen primarily to examine the complex chemistry of the site, where interactions between organics and liquid water likely occurred within the impact melt (Lorenz et al. 2021).

Selk is an impact crater that measures approximately 90 km in diameter with water-rich material potentially exposed in and around the crater and its ejecta, and a complex impact-induced and post-impact geology (Soderblom et al. 2010; Lorenz et al. 2021). It was best observed by VIMS during Titan's flybys T35, T38, and T40 (Soderblom et al. 2010). Among all the VIMS observations of the Selk crater area, we selected four cubes that allow us to map the region with the best compromise between spatial coverage and spatial sampling. The main characteristics of the four selected VIMS data cubes are presented in Table 3. Due to uncertainties in the navigation, the

Table 3
Main Characteristics of the Four Selected VIMS Data Cubes over the Selk Crater Area Ordered by Decreasing Spatial Sampling

VIMS Cube ID	Size (pixel × pixel)	Titan Flyby	Acquisition Date	Spatial Sampling (km pixel ⁻¹)	Phase Angle (°)	Incidence Angle (°)	Emission Angle (°)
CM_1578266417_1	64 × 64	T40	01/05/2008	11.4–12.9	52.1–54.5	23.8–44.2	9.2–33.0
CM_1575509158_1	64 × 64	T38	12/05/2007	6.4–7.4	40.6–43.0	25.2–37.7	9.6–29.8
CM_1578263500_1	64 × 64	T40	01/05/2008	3.4–4.4	38.4–44.5	29.2–35.5	7.4–19.6
CM_1578263152_1	64 × 64	T40	01/05/2008	2.5–3.4	31.7–40.3	30.0–35.1	9.2–16.9

four cubes have been co-registered as was done in Soderblom et al. (2010). Taking the map with the largest spatial sampling as a reference, we performed the coregistration by defining manually ground control points and applying a classic rotation–scaling–translation warping and bilinear resampling to the three other maps. Figure 12 shows the final projected mosaics built with the four co-registered cubes in the first available atmospheric band and window, along with the RGB color composite of single bands and band ratios, and the corresponding viewing geometry and spatial sampling.

4.2. Surface Albedo Maps of the Dragonfly Landing Area

Merging Titan’s orbital observations acquired in different viewing conditions into homogeneous mosaics is challenging due to the nonisotropic photometry of the atmosphere and surface (e.g., Le Mouélic et al. 2012; Le Mouélic et al. 2019). This is noticeable in our case (Figure 12), where systematic and significant seams (i.e., abrupt changes in I/F) are clearly visible at the transitions between the four VIMS data cubes of our mosaic, not only in atmospheric bands (e.g., Figure 12(a)) but also in atmospheric windows (e.g., Figure 12(b)). The four data cubes have been acquired in a short time interval (within an Earth-month between T38 and T40 observations, and within 1 hr for T40 observations) so that we can make the reasonable hypothesis that the atmosphere and surface properties did not change significantly. Hence, the seams are mainly originating from the varying viewing geometries (Figures 12(g), (h), and (i)) that our RT model should be able to account for or at least mitigate.

We inverted haze and mist scaling factors and surface albedos for all the pixels of the four VIMS data cubes with the RT-IPGP-2022 model. This represents a total of 16,384 pixels to be processed and two continuous weeks of parallel computations on a 40 core workstation.

We present the first part of the results in Figure 13, which are the haze and mist scaling factor maps over the Selk crater area. The I/F mosaic at 0.88 μm (Figure 13(a)), in the first atmospheric band available in the VIMS-IR channel, is strongly heterogeneous, presenting marked I/F slopes within each individual data cube and notable I/F value discrepancies between the data cubes, all correlated with the viewing geometries (see Figure 12). The F_h mosaic (Figure 13(b)), and the F_m mosaic (Figure 13(c)) to a lesser extent due to greater uncertainties in F_m retrievals, is significantly more homogeneous. F_h and F_m mosaics do not present any global trends with viewing geometry, and seams between VIMS data cubes are significantly reduced and even disappear at most of the data cube transitions.

Once the haze and mist opacities are constrained, we can retrieve the surface albedos in the atmospheric windows for the four VIMS cubes used in this study. The results are shown in Figures 14 and 15. Although seams have been mostly mitigated

for the haze and mist maps, some residual seams still appear in surface albedo mosaics (Figures 14 and 15, middle row). Since atmospheric contributions are correctly evaluated by our RT model, these remaining seams are likely to be mainly due to the possible anisotropic photometric properties of the surface not taken into account in the model. We therefore apply a photometric correction inspired by the one used for the DISR spectrum of the HLS (see Section 3.3.2) that takes into account the dependency of the surface photometry on both the phase (g , expressed in radians) and incidence (i) angles in the form $a g^\beta / \cos(i)$, with β the phase exponent and a a constant. β is set free and has to be adapted to the type of surface that is observed. We found that the phase exponent value that best reduces the seams on the surface albedo mosaics of the Selk crater region is $\beta = 0.3$. We scale our correction to an existing observing case having $g_{\text{ref}} = 40^\circ$ and $i_{\text{ref}} = 34^\circ$, which are the mean observed phase and incidence angles of the studied cubes so that $a = 1 / (g_{\text{ref}}^{0.3} / \cos(i_{\text{ref}})) = 0.92$. We show in Figures 14 and 15 (bottom row) the surface albedo mosaics after the photometric correction. The remaining seams are still discernible in the 0.94 μm surface albedo mosaic, certainly due to residual atmospheric contributions (at a wavelength highly sensitive to aerosol scattering). The surface albedo mosaics in all the other atmospheric windows present a significantly higher degree of homogeneity, with drastically reduced seams and enhanced contrast, with respect to I/F and uncorrected surface albedo mosaics.

In order to discuss more quantitatively the quality of our retrievals for the haze and mist opacities and surface albedos, we extract and compare the behavior of I/F at 0.88 μm and 1.07 μm with one of F_h , F_m , and surface albedos along longitudinal transects at four different latitudes where the VIMS cubes are overlapping (Figure 16). Incidence, emission, and phase angles are also indicated along the same transects.

On the 0.88 μm I/F transects (see Figure 16, second row), we can clearly see a low-spatial-frequency, positive $\approx 20\%$ – 25% slope across a ≈ 1000 km distance toward the east. This positive slope is directly correlated with and can be fully explained by both decreasing incidence and increasing emission angles along the transects (see Figure 16, first row). I/F value discrepancies of $\approx 5\%$ – 12% are also strikingly visible at VIMS data cube transitions. They are all due to sudden changes in viewing geometries between data cubes (see Figure 16, second row). All this shows that these I/F variations are not physical and exclusively originate from varying viewing geometries within and between data cubes. This is further confirmed when we look at the corresponding F_h and F_m transects (see Figure 16–third row), which are physical values related to the haze and mist opacities. Here, slopes and seams totally vanish, becoming both less than the 2σ uncertainties of the F_h and F_m retrievals. The inversion of F_m is more uncertain, being performed within fewer VIMS spectels. This results in greater variability in F_m

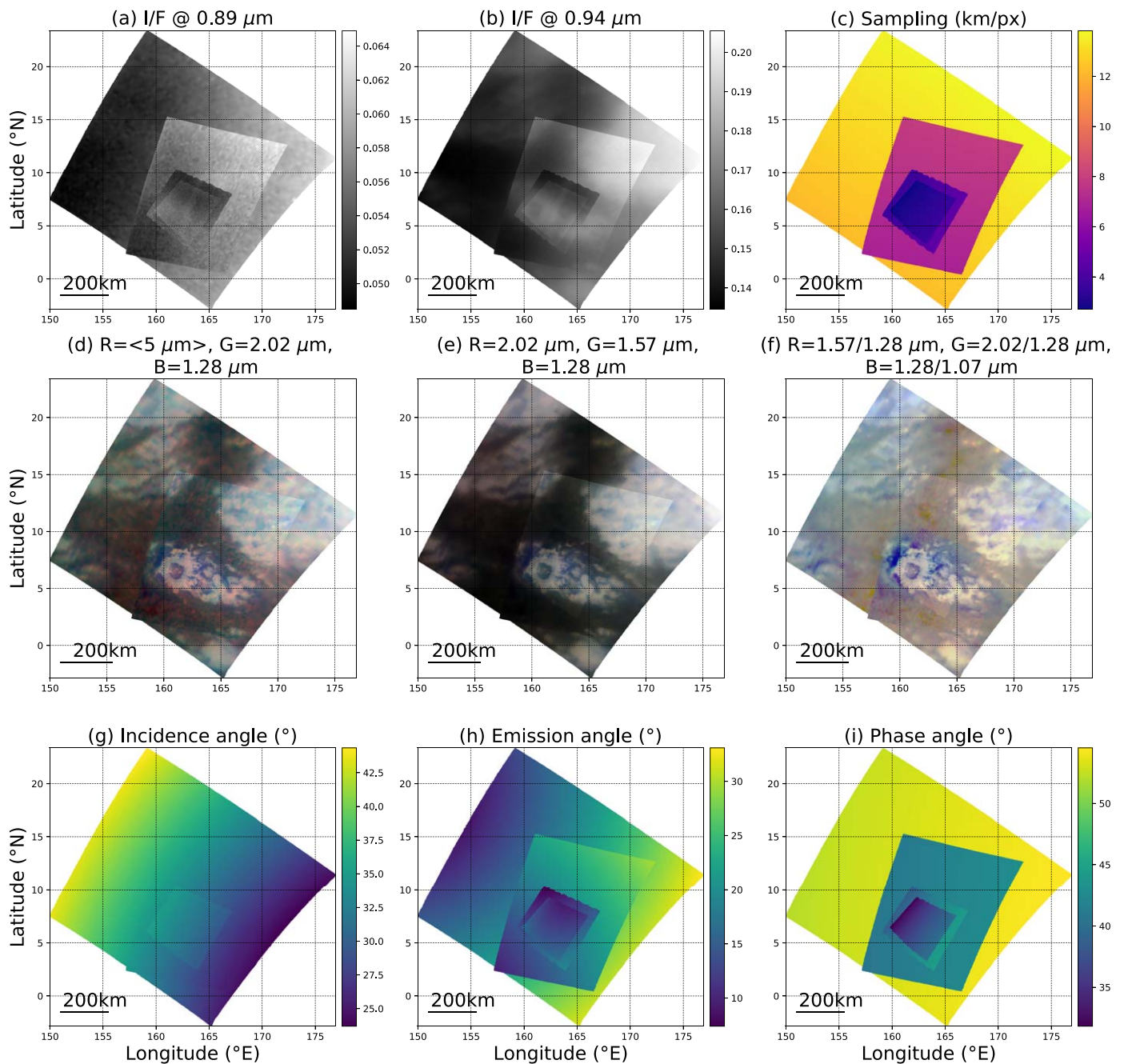


Figure 12. Mosaics of the four selected (and co-registered) VIMS cubes over the Selk crater area: (a) I/F at $0.89 \mu\text{m}$, (b) I/F at $0.94 \mu\text{m}$, (c) spatial sampling in km pixel^{-1} , (d) RGB color composite with $R = (5 \mu\text{m})$, $G = 2.02 \mu\text{m}$, and $B = 1.28 \mu\text{m}$ (Barnes et al. 2007), (e) RGB color composite with $R = 2.02 \mu\text{m}$, $G = 1.57 \mu\text{m}$, and $B = 1.28 \mu\text{m}$ (Soderblom et al. 2010), (f) RGB color composite with $R = 1.57/1.28 \mu\text{m}$, $G = 2.02/1.28 \mu\text{m}$, and $B = 1.28/1.07 \mu\text{m}$ (Le Mouélic et al. 2019), (g) incidence angle, (h) emission angle, and (i) phase angle. The mapping projection is rectangular with grid marks every 5° of longitude and latitude. Longitude is in degrees east.

values and 2σ uncertainties. Nevertheless, even the F_m transects are compliant with no slope and seams within the 2σ uncertainty interval.

I/F transects at $1.07 \mu\text{m}$, in an atmospheric window, present value discrepancies of $\approx 5\%$ – 10% at VIMS data cube transitions (Figure 16-fourth row). If a few can be attributed to natural albedo contrasts at the transition between different surface terrains, most of them are artifacts due to Titan’s atmosphere and surface photometry. Although atmospheric contributions were mostly taken into account by our RT model, the corresponding surface albedo transects at $1.07 \mu\text{m}$, not

corrected for the surface observing conditions (Figure 16, fifth row, blue curve) also show remaining small, but abrupt, value discrepancies of $\approx 5\%$ – 10% at a few data cube transitions. Even if the albedo discrepancies are subtle, much less than the retrieved uncertainties on the surface albedos, they are perfectly discernible on the mosaics (Figures 14 and 15, middle row). When corrected for the observing geometry, those discrepancies are drastically reduced to only a fraction of a percent (Figure 16, fifth row, red curve), replaced by smooth albedo transitions. In the end, this confirms at a much larger spatial scale what we already assessed for one pixel at the HLS. The

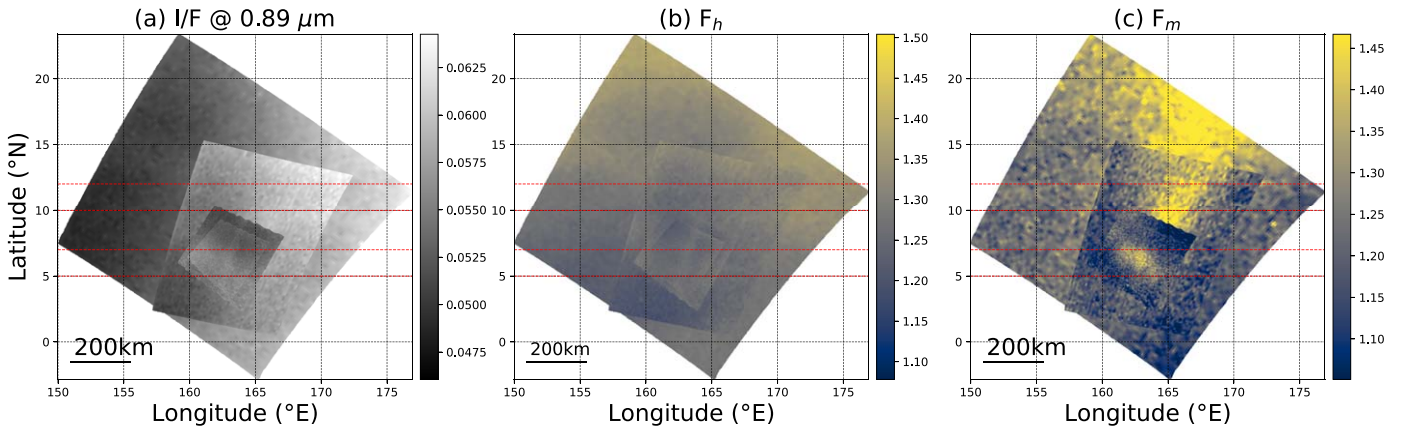


Figure 13. Mosaics of the four selected (and co-registered) VIMS cubes over the Selk crater area: (a) I/F at $0.88 \mu\text{m}$, (b) retrieved haze scaling factor F_h , and (c) retrieved mist scaling factor F_m . For comparison, the same 33% relative dynamics range values are applied for the three mosaics. The mapping projection is rectangular with grid marks every 5° of longitude and latitude. Longitude is in degrees east. We extract I/F , F_h , and F_m transects along the four horizontal red lines indicated on the $0.88 \mu\text{m}$ I/F , F_h , and F_m mosaics (see Figure 16).

RT-IPGP-2022 model provides an excellent correction for atmospheric haze and mist contributions and consequently a robust assessment of surface albedos, owing to a reliable surface photometry correction. The model can now be used iteratively on entire VIMS data cubes, and the resulting regional surface albedo maps can now be utilized with confidence, as a complement to geomorphological maps, for geological analyses.

4.3. Analyses of the Surface Albedos of the Dragonfly Landing Area

A routine extraction of the surface albedo in Titan's eight NIR atmospheric windows opens new perspectives for the study of Titan's complex geology and climatology. With the help of surface albedo estimations at the regional scale, we can define and map spectral ratios and spectral signatures directly sensitive to specific surface materials.

In the absence of wavelength-dependent offsets (e.g., atmospheric scattering), rationing the surface albedos obtained in different spectral bands, which aims at canceling out all multiplicative contributions (mainly albedo and viewing conditions), is a powerful technique to enhance subtle spectral heterogeneities in the near-infrared (e.g., Le Mouélic et al. 1999). These heterogeneities can be due to local changes in the composition and/or grain size of the surface material. For Titan, the VIMS $1.57/1.28$, $2.02/1.28$, and $1.28/1.07 \mu\text{m}$ band ratios proved to be useful for both regional and global studies by enhancing specific spectral units (e.g., bright, dark brown, dark blue) that can be associated with terrains composed in majority of small-sized solid organics (bright units), larger-grain organics (dark brown), or enriched in water ice grains (dark blue) (e.g., Rodriguez et al. 2006; Le Mouélic et al. 2008, 2019; Brossier et al. 2018). We show in Figure 17(a) the RGB color composite mosaic of the ratios of the surface albedos of the Selk crater region retrieved with our RT-IPGP-2022 model, with the $1.57/1.28 \mu\text{m}$ ratio for the red channel, $2.02/1.28 \mu\text{m}$ ratio for the green channel, and $1.28/1.07 \mu\text{m}$ ratio for the blue channel.

We also define a spectral index δ sensitive to the presence of surface material compatible with the spectrum of water ice, directly inspired by the work of Coutelier et al. (2021). Because the VIMS spectral sampling and resolution are insufficient to

resolve narrow, specific absorption bands within the atmospheric windows, this index is not used to firmly detect water ice but rather highlights where spectra are consistent with the behavior of a surface unit enriched in water ice. The index is based on a combination of spectral ratios at specific wavelengths of water ice absorption that occur within the surface windows. It is built as the one of Coutelier et al. (2021), except that we do not use the albedo level in the $5 \mu\text{m}$ window for consistency, as it is not based on a spectral ratio. The spectral ratios are

1. $r_1 = 1.58/1.28 \mu\text{m}$
2. $r_2 = 2.02/1.28 \mu\text{m}$
3. $r_3 = 2.02/1.58 \mu\text{m}$
4. $r_4 = 2.70/2.78 \mu\text{m}$.

These ratios are then normalized as

$$r_{i,n} = \frac{r_i - r_{i,\min}}{r_{i,\max} - r_{i,\min}},$$

with $r_{i,\min}$ and $r_{i,\max}$ the minimum and maximum values of the ratio for the considered cube. Normalized ratios are subtracted (i.e., r_1 , r_2 , r_3) or added (i.e., r_4) to the index if the expected nonnormalized-ratio values are higher or lower than 1, respectively. The ratios are weighted by their uncertainties, such as for a ratio r of surface albedos A_i and A_j , the relative uncertainty is

$$\sigma = \frac{\Delta r_i}{r_i} = \frac{\Delta A_i}{A_i} + \frac{\Delta A_j}{A_j},$$

with ΔA the 1σ uncertainty on the surface albedo. Finally, the index δ is

$$\delta = -\sum_{i=1}^3 (1 - \sigma_i) r_{i,n} + (1 - \sigma_4) r_{4,n}. \quad (8)$$

The higher this index, the greater the surface enrichment probability in water ice.

This criterion is already proved to give consistent results. It was previously used in the southern part of the Xanadu region (Coutelier et al. 2021), where its highest values were found to

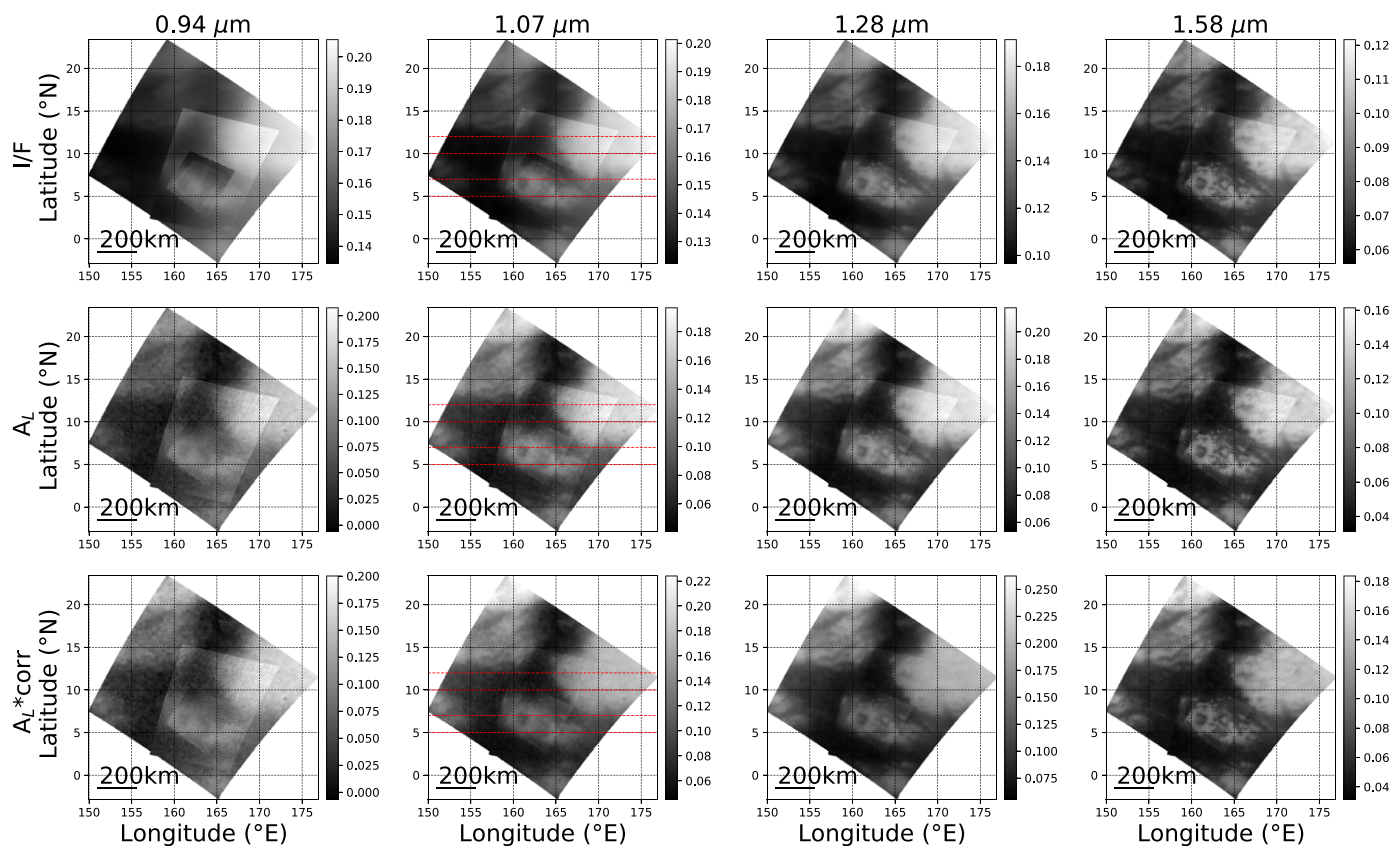


Figure 14. Mosaics of the four selected (and co-registered) VIMS cubes over the Selk crater area in the four first atmospheric windows: (top row) I/F , (middle row) direct output of our RT model, i.e., Lambertian surface albedo, and (bottom row) Lambertian surface albedo corrected for surface photometry. The mapping projection is rectangular with grid marks every 5° of longitude and latitude. Longitude is in degrees east. We extract I/F , uncorrected, and corrected surface albedo transects along the four horizontal red lines indicated on the $1.07 \mu\text{m}$ I/F mosaics (see Figure 16).

be spatially correlated with geomorphological units supposed to be enriched with surficial water ice (as grains or cobbles mixed with other materials), such as the rivers and their mouths visible in the RADAR/SAR images that are supposed to be dried up and rich in water ice sediments (Le Gall et al. 2010). Conversely, Coutelier et al. (2021) also showed that the index has its lowest values at places where organic sediments are supposed to dominate the surface composition (such as hills and plains). We calculated this “water ice enrichment” index for the entirety of the Selk crater area mosaic with the help of the surface albedos retrieved with our RT-IPGP-2022 model. The “water ice enrichment” index map is shown in Figure 17(b).

The two mosaics—the RGB of spectral ratios and the “water ice enrichment” index—can be jointly analyzed in terms of surface composition and granulometry and linked to the local geomorphology in order to help to better understand the formation and evolution of the landscapes and their possible connection with the local climatology. We superimposed the geomorphological unit map of Lorenz et al. (2021) (Figure 17(e)) on both the RGB and “water ice enrichment” index mosaics (Figures 17(f) and (g)). This geomorphological classification map was built by classifying the different types of terrains that have been identified on the high-resolution Cassini/Synthetic Aperture Radar (SAR) mosaic of the Dragonfly landing area.

In the classification map of Lorenz et al. (2021) (Figure 17(e)), five major types of terrains have been identified: (1) the Selk crater rim, bright and highly textured in SAR

images, (2) the crater floor and (3) the ejecta blanket, both as bright with no slope texture in SAR images, (4) SAR-dark dunes with SAR-bright interdunes, and (5) SAR-dark terrains compatible with sand but no obvious dunes at the SAR resolution. These terrains are spatially correlated with infrared albedo units, even if only partially at some places due to differences in the penetration depth into the surface material between the RADAR and infrared observations and due to sensitivity to different scales of roughness. On the RGB mosaic of surface albedo band ratios (Figures 17(a) and (c)), several spectral units readily show up with a high degree of spatial consistency: a yellow-bright unit, a unit constituted with a mix of brown and blue, a purple unit, and a dark-blue unit among the most obvious.

The infrared yellow-bright unit is associated with the crater rim and ejecta, and the elevated terrains to the northeast. The lowest values of the “water ice enrichment” index are highly spatially correlated with this spectral unit. The index is all the lower as the yellow-bright unit is light. The yellow-bright spectral unit, associated with a low index, is indicative that these terrains are strongly depleted in water ice and likely to be dominated by complex organics, at least superficially.

The dunes and SAR-dark terrains with no obvious dunes but compatible with sand cover the largest area around the Selk crater and are very well correlated with the infrared brown-blue unit. This unit presents a quasi-uniform “water ice enrichment” index with low to intermediate values, compatible with a possible moderate content in water ice. The most likely explanation is that those terrains are a geographic mixture of

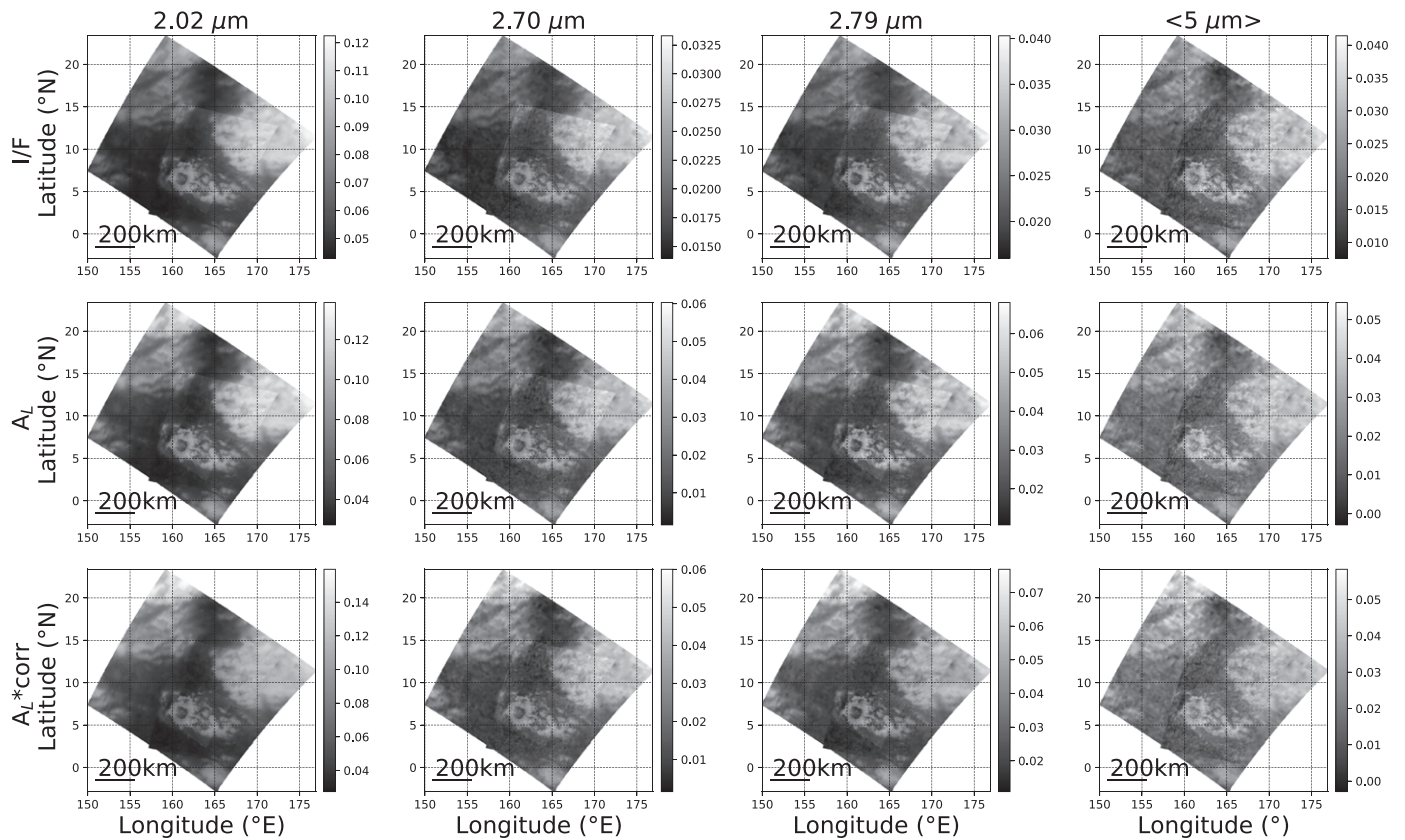


Figure 15. Mosaics of the four selected (and co-registered) VIMS cubes over the Selk crater area in the four last atmospheric windows: (top row) I/F , (middle row) direct output of our RT model, i.e., Lambertian surface albedo, and (bottom row) Lambertian surface albedo corrected for surface photometry. The mapping projection is rectangular with grid marks every 5° of longitude and latitude. Longitude is in degrees east. The $5\ \mu\text{m}$ window mosaics result from averaging over 15 VIMS spectels from 4.89 to 5.13 μm to increase the S/N.

dunes of organic sand and interdunes where the icy bedrock can be sparingly exposed, as suspected by the thorough examination of the SAR images (Barnes et al. 2021; Lorenz et al. 2021; Bonnefoy et al. 2022).

The infrared purple unit can be found locally within the crater ejecta and floor, and as patches embedded in the yellow-bright terrains at the northeast of the mosaic. This unit is characterized by a “water ice enrichment” index higher than that of the brown-blue unit. It can be interpreted as terrains where organic sand and icy bedrock also cohabit with probably a higher content in water ice than for the dune fields outside the crater. This hypothesis is supported by the few dunes observed within the SAR-brighter crater floor in the higher-resolution SAR images (Barnes et al. 2021; Lorenz et al. 2021; Bonnefoy et al. 2022).

Finally, the infrared-dark blue unit, visible only as very localized patches right at the north, east, southwest, and northwest of the crater rim, is strongly correlated with the highest “water ice enrichment” index. This spectral behavior is in accordance with what was already reported by, e.g., Brossier et al. (2018), being possibly indicative of the strongest content in water ice in the investigated VIMS data cubes.

We show in Figure 18 the retrieved surface albedo corrected for the photometry in the center of the atmospheric transmission windows for the four most prominent spectral units revealed in the RGB map (i.e., brown-blue, purple, dark-blue, and yellow-bright units). Each spectrum is the average of a selection of pixels within each unit with 1σ mean arithmetic uncertainties. The $5\ \mu\text{m}$ window results from averaging over 15

VIMS spectels from 4.89 to 5.13 μm to increase the signal-to-noise ratio (S/N). Despite the absence of obvious absorption bands and large error bars at short wavelengths, differences are clearly visible, both on the global albedo level and on spectral slopes in specific wavelength regions. The yellow-bright unit is the brightest in all windows, followed by the purple unit. The brown-blue unit is the darkest in the first three windows and is the only unit to display an almost one-to-one ratio for the 1.57 and 2.02 μm windows. Within the error bars, the 2.70/2.79 μm ratio of the dark-blue unit and its low albedo at 5 μm are the most consistent with a possible enrichment in water ice (e.g., Rodriguez et al. 2006; Soderblom et al. 2007; Barnes et al. 2008; Brossier et al. 2018; Coutelier et al. 2021). From these albedo spectra, by considering more spectels sensitive to surface contribution within the atmospheric transmission windows, not only the center, it may be possible to more directly estimate the most probable superficial composition and granulometry. It would require new developments and is out of the scope of the present study.

Putting this new set of observations together and with the help of previous studies of the Selk crater region, including Cassini VIMS, RADAR SAR, radiometry, and SAR-topo data (e.g., Soderblom et al. 2010; Werynski et al. 2019; Barnes et al. 2021; Lorenz et al. 2021; Bonnefoy et al. 2022), we can provide a possible scenario of the local geological and climatic history.

Owing to the relatively low RADAR emissivity seen in the radiometry observations (Werynski et al. 2019) and to the SAR backscattering (Bonnefoy et al. 2022), the Selk crater rim is

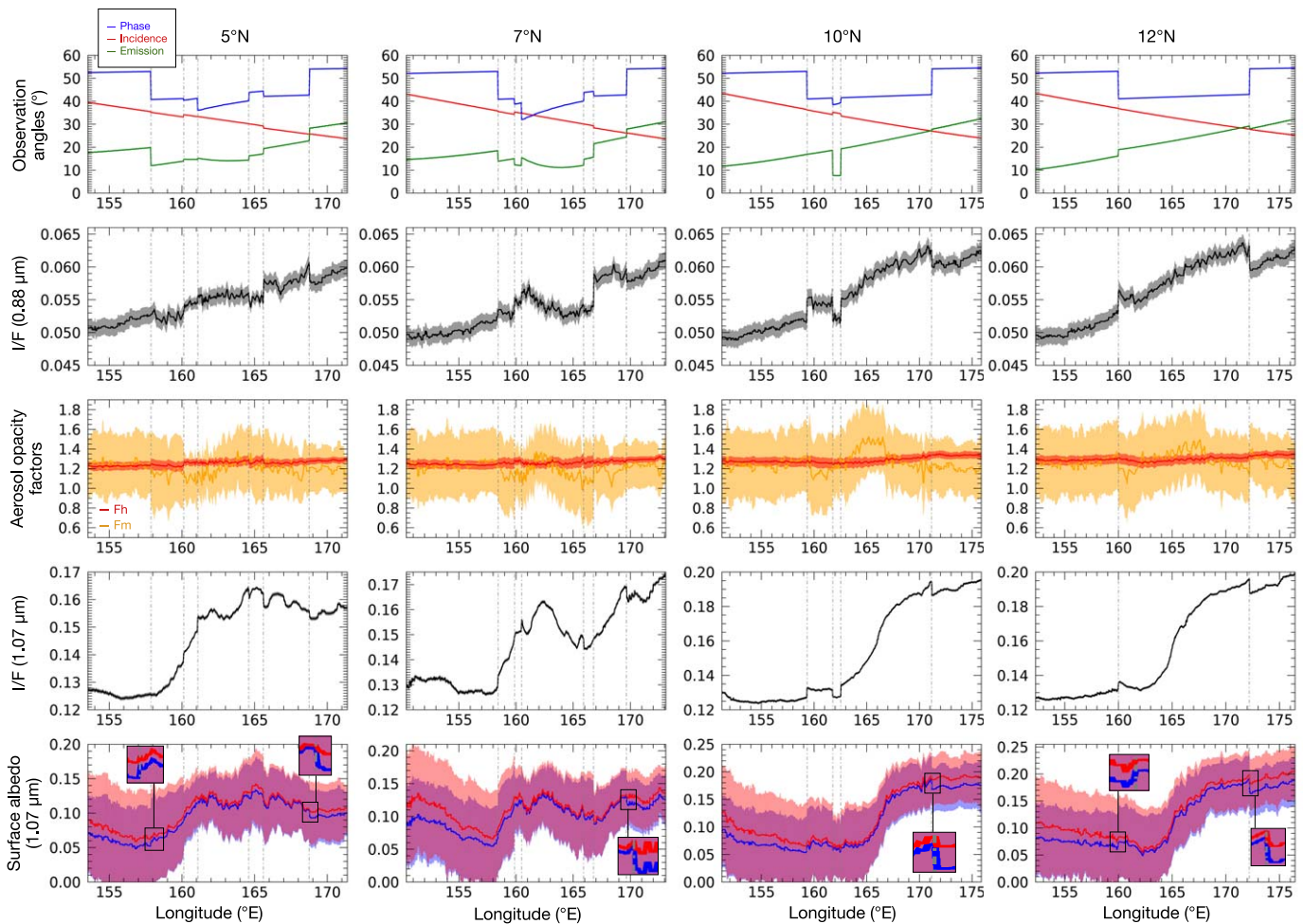


Figure 16. Longitudinal transects at four different latitudes (5°N, 7°N, 10°N, and 12°N) extracted from the VIMS mosaic of the Selk crater region (see Figures 13 and 14 and 15): (first row) incidence, emission, and phase angles, in red, green and blue, respectively, (second row) I/F in an atmospheric band, at 0.88 μm here, (third row) haze (F_h , red curve) and mist (F_m , orange curve) opacity factors, along with their 2σ uncertainty envelopes, (fourth row) I/F in an atmospheric window, here at 1.07 μm , and (fifth row) surface albedos at 1.07 μm , uncorrected (in blue) and corrected (in red) for surface photometry (see text for detailed explanations of the surface photometry correction), along with their 2σ uncertainty envelop. Zooms on a few transitions between VIMS data cubes are also provided. Gray dotted vertical lines correspond to cube transitions.

consistent with a higher water ice content, at least in the near subsurface. This is expected as crater rims are supposed to be windows into the crust composition. This is in apparent contradiction with what is inferred from the VIMS observations, which suggest a crater and its ejecta blanket rather dominated by tholin-like solid organics. The most likely explanation is that the rim and ejecta of the Selk crater are covered by a blanket of atmospheric organic fallouts, thin enough (from a few tens of micrometers to a few tens of centimeters) for the RADAR to be still sensitive to the water ice lying underneath. A possibility is that the Selk crater is old enough for its rim and ejecta to be already covered by a sufficient amount of organic sediment as seen by VIMS, but still young enough so that the sediment blanket is not too thick for the near-subsurface water ice (originally at the surface) to be seen by the RADAR radiometer and SAR. This is in agreement with the analysis of Werynski et al. (2019), who classified the Selk crater at an intermediate state of degradation. It is worth noting that the ejecta has a higher RADAR emissivity (Werynski et al. 2019) than the rim, while in the infrared (probing the very top subsurface) they both seem equally depleted in water ice, which can be explained by the

chaotic nature of those ejecta terrains constituted by a homogeneous mixture of water ice (ejected from the crust) and organic sediment at the surface and at depth.

At the center of the crater, the SAR images show the presence of a few RADAR-dark dunes, RADAR-bright interdunes, and slightly brighter areas, with a possible central peak (Werynski et al. 2019; Barnes et al. 2021; Lorenz et al. 2021; Bonnefoy et al. 2022). The RADAR emissivity, averaged over the entire crater floor, is higher than that of the rim but not as high as that of the neighboring dune fields or that of the interior of an older crater filled with dunes like Santorini (Werynski et al. 2019). Hence, if the crater floor might be covered by a thick bed of accumulated organic sediments—from where isolated dunes can develop—the SAR and radiometric data do not rule out ice outcropping from the crust in this region, in the interdunes and possibly at the central peak. This is in agreement with the relatively uniform infrared purple unit and higher “water ice enrichment” index of the crater floor.

At places around the rim of the crater, at the bottom of the slopes, and inside and outside the crater, we identify a few infrared-dark blue patches. These infrared units are found within the ejecta blanket unit with no distinct brightness or

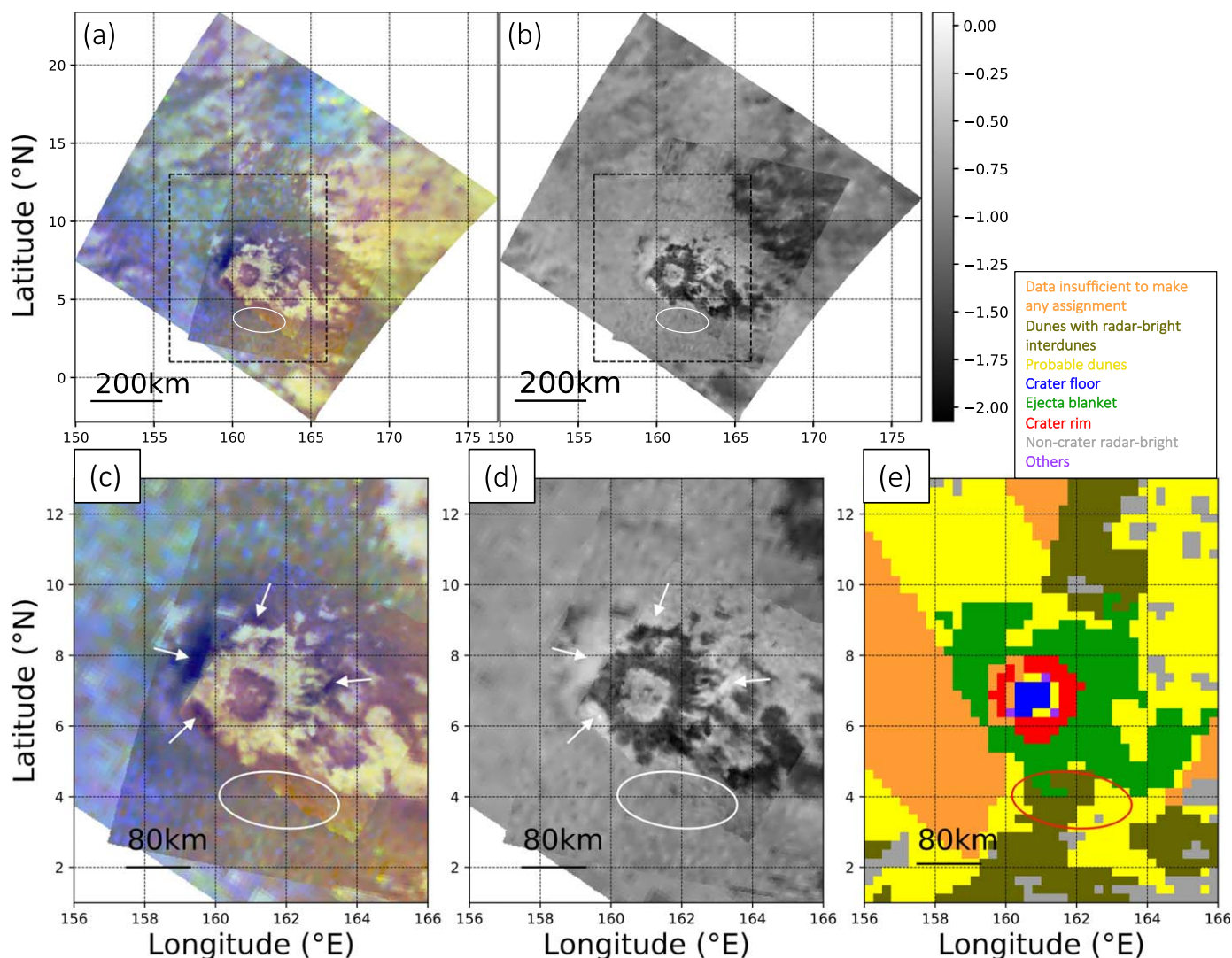


Figure 17. (a) RGB mosaic of the Selk crater region, with the $1.57/1.28 \mu\text{m}$ albedo ratio as the red channel, the $2.02/1.28 \mu\text{m}$ albedo ratio as the green channel, and the $1.28/1.07 \mu\text{m}$ albedo ratio as the blue channel. (b) Same mosaic for the “water ice enrichment” index. (c) and (d) Zooms on (a) and (b). (e) Classification map of the Selk crater region (Lorenz et al. 2021). The color legends are given in the frame above. White arrows designate the areas with the highest “water ice enrichment” index, corresponding to the dark-blue units on the RGB mosaic. The initial landing ellipse of Dragonfly is indicated by the solid oval on each map (Barnes et al. 2021).

texture in the SAR images. They may witness localized superficial deposits to which only the infrared wavelengths are sensitive. They are all strongly correlated to the highest “water ice enrichment” index of the area and may be witnesses of the local pluvial and fluvial activities, as suggested by Soderblom et al. (2010) and by Brossier et al. (2018) in an equivalent geological and climatic context. In particular, the spectral analyses of Brossier et al. (2018) indicated that these dark-blue units may be organic deposits particularly enriched with water ice pebbles. A mixture of fine-grain organics and larger-grain icy rocks may have been produced by the fluvial incision of the surface and near-subsurface substrates at higher altitudes, transported downwards by rivers and deposited in outwash plains as alluvial cones. At the north and east of the Selk crater rim, the SAR and VIMS images possibly reveal the presence of river valleys dissecting the crater rim (Soderblom et al. 2010). Rivers are also reported cutting the walls of the Forseti and Sinlap craters (Brossier et al. 2018; Werynski et al. 2019) and can be a common erosion feature on crater flanks. These river valleys are connected to two of the dark-blue units reported

here, in agreement with their fluvial erosion origin. The spatial resolution of the VIMS data cubes used in our study and the quality of our infrared albedo retrievals are good enough to even be able to see and follow the dark-blue unit along the narrow river valley of the north, strengthening our hypothesis. There may be more river valleys incising the crater walls, but SAR images of sufficient resolution are lacking in most of the area.

Those rivers may also be one of the modern sources of organic sediment that keep supplying the surrounding extensive dune fields. The spectral differences, and thus the color difference in the VIMS RGB mosaic, between the elevated terrains (yellow-bright) and most of the plains at the lowest altitudes (brown-blue), suggest that the sediment that covers the top centimeters of the rim and ejecta are likely to be different in granulometry, if not in composition, from the organic sand that composes the dunes. Indeed, Brossier et al. (2018) demonstrated in another equatorial region that, although being of similar chemical composition, the dune material in the topographic lows (infrared brown-blue) could be composed of larger grains than the fresher sediment (infrared yellow-

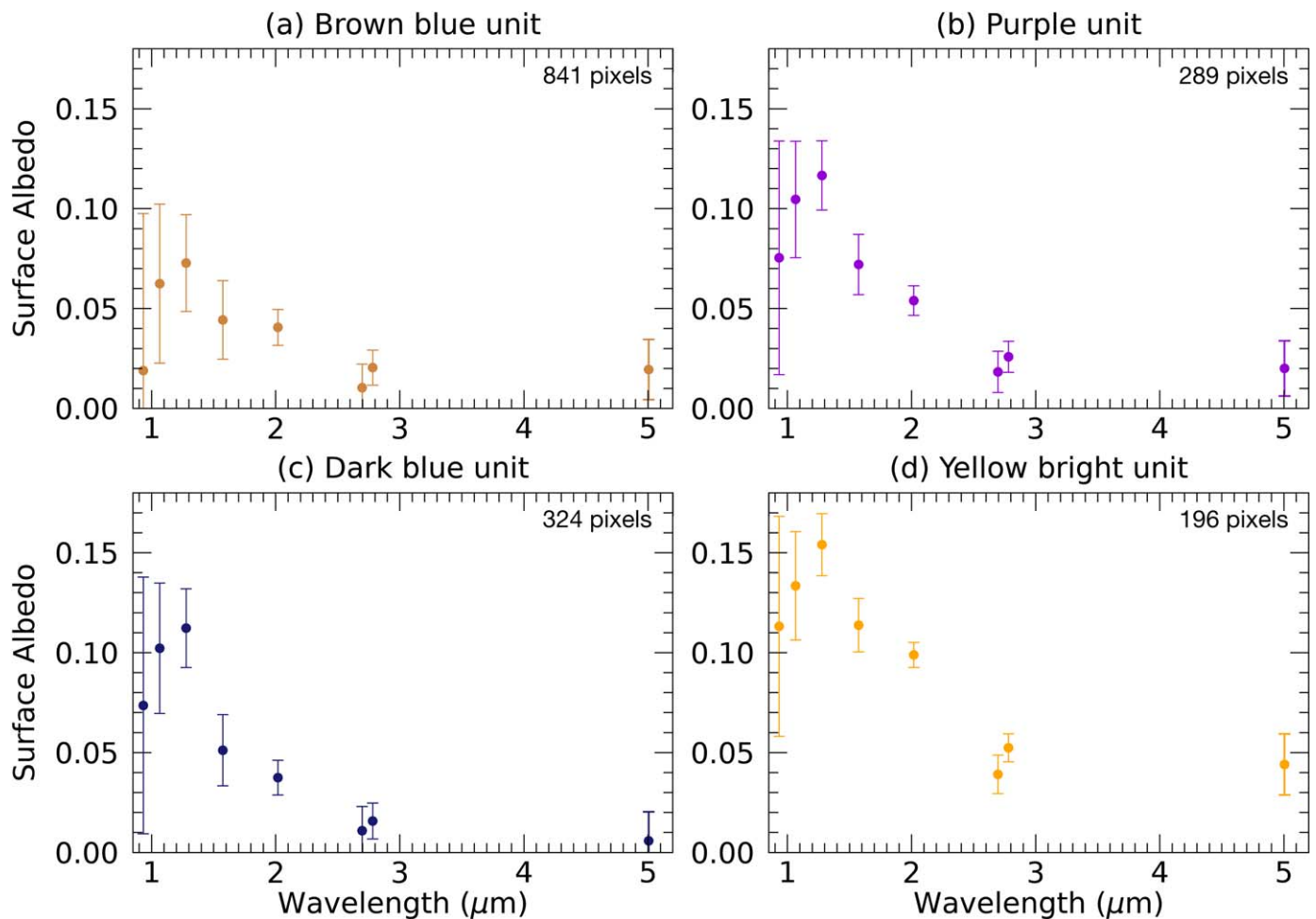


Figure 18. Retrieved surface albedo corrected for the photometry in the center of the methane windows for the four most prominent spectral units revealed in the RGB map: (a) brown-blue, (b) purple, (c) dark-blue, and (d) yellow-bright units. Each spectrum is the average of a selection of pixels within each unit (841, 289, 324, and 196 pixels, respectively) with 1σ mean arithmetic uncertainties. The 5μ window results from averaging over 15 VIMS spectels from 4.89 to 5.13 μm in order to reduce the noise. For comparison, the results are displayed over the same range of albedo values.

bright unit) that covers the more elevated, mountainous terrains. At the Selk crater, the fine-grain organic sediment can be swept from the crater rim by episodic rainfalls (Faulk et al. 2017), transported along with the water ice cobbles by the rivers incising the crater walls and deposited in the lowlands, farther than the water ice cobbles due to their lower mass. There, different episodes of transport and processing (sintering, lithification, flocculation) may enable the formation of larger grains that will be eroded by the winds and will help to supply the surrounding dune fields (Le Mouélic et al. 2008; Barnes et al. 2015; Neish et al. 2015).

It is important to put these results in context with observations of other impact craters on Titan. Although a thin layer of fine-grained atmospheric deposits is consistent with these observations of Selk, it does not explain the spectral signature of all impact craters on Titan. Notably, craters that are morphologically fresher (like Sinlap) and more degraded (like Soi) than Selk both show more evidence of superficial water ice in their rims and ejecta blankets (Solomonidou et al. 2020). This suggests there are active surface processes occurring on Titan to alter the infrared spectral signatures of impact craters over time. It may be that fresher craters (like Sinlap) have not had time to acquire a consistent layer of fine-grained organics on their rough, blocky rims and ejecta. Over time, the fine-

grained organics may build up, while the rim and ejecta will become smoother due to fluvial erosion, producing a more consistent layer of organics seen by VIMS. Given more time and adequate meteorological conditions (i.e., increased rainfall in the plains), these fine-grained organics may be washed away to produce an infrared spectral signature more enriched in water ice, as we see at the Soi, Sinlap, or Afekan craters (Werynski et al. 2019; Solomonidou et al. 2020). Thus, the Selk crater may represent part of a continuum of spectral signatures expected for impact crater rims; these ideas will be directly testable with observations by Dragonfly.

We identify a certain number of interesting targets in and around the Selk crater for the future exploration plans of Dragonfly. First of all, there are targets of prime astrobiological interest, at the crater rim and floor, where interactions between organics and liquid water likely occurred within the impact melt. We propose for instance to sample the interdune material, any remnants of a central peak, and icy material transported by rivers from the crater rim to the crater floor (Neish et al. 2018). These terrains all appear to have material coming from the crust transformed by the impact and probably mixed with surface organics if dunes or organic sediment were present before the impact. There are also targets of prime geological and climatic interests. Imaging and possibly sampling the grain size and

composition of the sediment, from the top of the crater rim to the alluvial cones, would help us better comprehend the erosional history, the climate, and the formation of the landscapes of the Selk crater area and serve as a proxy for the entire equatorial region of Titan.

5. Conclusion

We present in this study significant improvements applied to our radiative transfer model for Titan’s atmosphere and surface. Our model is designed to simulate the observations of Titan realized by the VIMS instrument on board the Cassini spacecraft and for future similar measurements. The new iteration of our model (RT-IPGP-2022) takes advantage of the most recent updates for both the gas and aerosol descriptions, notably the gaseous absorption line lists, the gas volume mixing and isotopic ratios, and the vertical distribution of aerosol optical properties. We opted for a general description of the aerosols by the use of an aggregate model calculating the vertical extinction profile, single-scattering albedo, and single-scattering phase function of fractal particles. We developed an inversion scheme that allows us to estimate the haze and mist opacities from the radiance factor in the NIR atmospheric bands, the surface albedo in the atmospheric windows, and their associated propagated uncertainties.

We validated the new version of our model and its updated description of Titan’s atmosphere with the help of in situ Huygens measurements of both the atmosphere and the surface, and VIMS orbital observations of the HLS. Our new model, constrained with the VIMS observations, is able to reproduce the spectral observations of the ULIS, part of the Descent Imager/Spectral Radiometer (DISR), during the descent of the Huygens probe over a great range of different altitudes (140 km down to the surface). Our model also manages to simulate Titan’s surface reflectivity spectrum recorded by DISR once Huygens landed. The RT-IPGP-2022 version of our RT model presents significantly better matches with Huygens measurements than our previous one (RT-IPGP-2016 model).

Once validated, we applied our model to the Selk crater region, near the site chosen for the landing of the future Dragonfly mission, in order to retrieve the infrared surface albedo at the regional scale and analyze the area in terms of geology and climatology. For our analyses, we selected four VIMS data cubes that offer the best trade-off between spatial coverage of the Selk crater region and spatial sampling. We use our RT-IPGP-2022 model to invert our entire VIMS mosaic of the Selk crater area (constituted of the four data cubes) for aerosol populations and surface albedos. Although VIMS mosaics present significant seams due to changing viewing conditions between the four observations, our inversions lead to the production of seamless aerosol distribution and surface albedo maps, owing to the use of a relevant surface photometric correction, further validating our model. We can use the surface albedo maps computed by our model with a higher degree of confidence to build analytical tools for the analysis of the surface composition and granulometry of the Selk crater region, like a map combining spectral ratios of surface albedos and a map showing the “water ice enrichment” index adapted from Coutelier et al. (2021). The spectral ratios and index maps allow us to distinguish surface units of different spectral behaviors and give hints to possible local enrichments in water ice. Putting together our results with the previous analyses of the extensive Cassini data set over the Selk crater region, we

are able to propose detailed geological and climatic scenarios that best explain all the observations. We suggest that the Selk crater is in an intermediate state of degradation. We suggest that heights and mountainous terrains (including rim and ejecta) are likely to be dominated by atmospheric deposits of fine grains of tholin-like sediment. This organic sediment would be transported to the lowlands (crater floor and surrounding plains), possibly with water ice particles, by rivers incising down near the water ice bedrock, and further deposited and processed to form the sand particles that feed the neighboring extensive dune fields. We thus identify specific targets of astrobiological and geological interests for the future exploration of this region by the Dragonfly rotorcraft.

Our model and methods, now validated and reproducible, can be widely used on the complete VIMS-IR data set to provide crucial information on Titan’s aerosol population, surface albedo, and composition at a global scale. Presently, the computation time of our RT model is too high to envisage such applications. But, we are working on drastically reducing the computation time (days rather than years), thanks to pre-calculated look-up tables (Rodriguez et al. 2021), enabling a new era in Titan exploration. Moreover, our model, designed for VIMS, can be adapted to analyze any ground- and space-based IR observations, especially the James Webb Space Telescope imaging and spectro-imaging observations. With a 10 times higher spectral resolution than VIMS in the near-infrared range, it will bring new constraints on Titan’s surface composition in the atmospheric windows, owing to surface albedo inversions that we can now provide with our RT-IPGP-2022 model.

This work was supported by CNES (Centre National d’Études Spatiales), Programme National de Planétologie of the Institut National des Sciences de l’Univers/Centre National de la Recherche Scientifique and ANR (Agence Nationale de la Recherche) project RaD³-net (ANR-21-CE49-0020). We thank B. Seignovert for Cassini VIMS cube coregistration, Sandrine Vinatier for discussions, and two anonymous reviewers for their helpful suggestions and very constructive criticism that greatly improved the quality of the final manuscript.

Data Availability

The data and radiative transfer results for this study are available at https://zenodo.org/record/7645466#.Y-3q_S8w07g, doi: 10.5281/zenodo.7645466.

Code Availability

The radiative transfer codes used can be accessed from the corresponding author upon request.

Appendix A On the Radiometric Noise of VIMS

VIMS radiometric noise is estimated for each spectral. We calculate the shot noise on the signal (S_s) and shot noise on the background (S_B , i.e., the dark) to determine the total shot noise ($S_{\text{tot}}(\lambda) = \sqrt{S_s^2 + S_B^2}$). The shot noise on the signal s is $S_s(\lambda) = \frac{\sqrt{s(\lambda)G + B(\lambda)G}}{G}$, with $s(\lambda)$ the uncalibrated signal in DN as a function of wavelengths, $B(\lambda)$ the mean background of the scan line as a function of wavelengths, and G the VIMS gain equals 300 DN^{-1} . The shot noise in the background is

$S_B = \frac{\sqrt{B(\lambda)G}}{G}$. The background signal $B(\lambda)$ of each scan line is extracted from the raw cube (*QUB). The 1σ total noise N in DN is thus defined as follows: $N(\lambda) = \sqrt{S_{\text{tot}}(\lambda)^2 + R^2}$, with R the read noise (equals to 1 DN for each VIMS spectel), i.e., the amount of noise generated by electronics as the charges present in the pixels are transferred to the camera. Finally, the 1σ standard deviation on the radiance factor is

$$\sigma(\lambda) = N(\lambda) \frac{f hc}{\tau \lambda} \frac{1}{A \Omega \delta \lambda} \frac{1}{F_{\odot, \lambda} d^2},$$

with f the VIMS transfer function in photon per DN, τ the exposure time in s, h the Planck constant in J, c the speed of light in m s^{-1} , λ the wavelength in m, A the VIMS-IR telescope aperture in m^2 , Ω the solid angle subtended by VIMS-IR IFOV, $\delta \lambda$ the VIMS spectels FWHM, $F_{\odot, \lambda}$ the Sun radiance factor in $\text{W m}^{-2} \mu\text{m}^{-1} \text{sr}^{-1}$, and d the Sun–Saturn mean distance in au.

Appendix B

Altitudes Probed by the VIMS Spectels: Selection for Haze–Mist Population and Surface Albedo Inversions

The effective opacity, written as $\tau^* = \tau \sqrt{(1 - \omega)(1 - \omega g)}$ (e.g., Pollack & McKay 1985; Rannou et al. 2003), where τ is the atmospheric opacity, ω the atmospheric single-scattering albedo, and g the atmospheric asymmetry factor, accounts for

the fact that forward scattering increases the photons’ mean free path. In the case of an optically thick atmosphere, transmission windows can be defined as the wavelengths where the cumulative effective opacity does not reach unity before the surface. Elsewhere, the altitudes where the cumulative effective opacity reaches unity give good estimators of the minimum altitudes probed by incident photons.

The cumulative effective opacity of Titan’s atmosphere can be calculated as a function of altitude for each of the 256 spectels of the VIMS-IR channel. We plot the altitudes where it reaches unity as a function of VIMS-IR wavelengths (Figure 19). This allows us to quantitatively estimate and select the VIMS-IR spectels that probe down to Titan’s surface (“surface spectels”) and those totally insensitive to the surface’s signal while probing the lowest possible altitude, here 10 km—the lowest level of the altitude grid of our RT model, removing methane absorption wings (“haze/mist spectels”). These spectels can be used to independently invert the surface albedo and haze/mist population. Surface spectels correspond to VIMS wavelengths of 0.933, 1.065 to 1.082, 1.278 to 1.295, 1.540 to 1.602, 2.002 to 2.100, 2.681 to 2.799, and 4.889 to 5.122 μm . Haze/mist spectels correspond to 0.884, 0.982 to 1.015, 1.130 to 1.196, 1.327 to 1.442, 1.656 to 1.853, and 2.167 to 2.615 μm (and not beyond due to VIMS’ low S/N). It should be noted that we do not use spectel 46 (1.6416 μm) because it is located at a filter gap between two detectors and is thus not reliable (Brown et al. 2004; Clark et al. 2018).

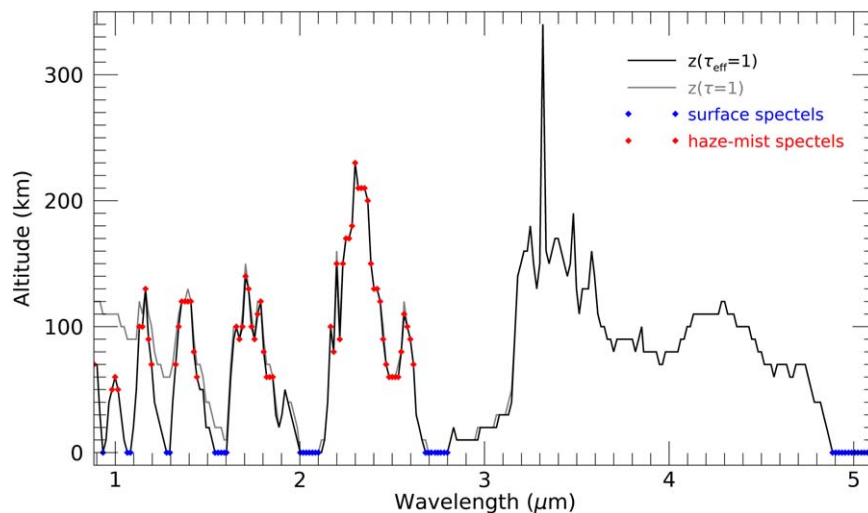















Figure 19. Altitudes where $\tau = 1$ (gray) and $\tau_{\text{eff}} = 1$ (black) vs. wavelengths. Red rectangles indicate the VIMS spectels used to invert the haze and mist scaling factors (“haze/mist spectels”) and blue rectangles the VIMS spectels used to invert the surface albedo (“surface spectels”).

ORCID iDs

M. Es-sayeh  <https://orcid.org/0000-0002-0643-4323>
 S. Rodriguez  <https://orcid.org/0000-0003-1219-0641>
 M. Coutelier  <https://orcid.org/0000-0002-0776-2732>
 P. Rannou  <https://orcid.org/0000-0003-0836-723X>
 B. Bézard  <https://orcid.org/0000-0002-5433-5661>
 T. Cornet  <https://orcid.org/0000-0001-5971-0056>
 E. Karkoschka  <https://orcid.org/0000-0002-4165-0064>
 S. Le Mouélic  <https://orcid.org/0000-0001-5260-1367>
 A. Le Gall  <https://orcid.org/0000-0002-9023-4868>
 C. Neish  <https://orcid.org/0000-0003-3254-8348>
 S. MacKenzie  <https://orcid.org/0000-0002-1658-9687>
 C. Sotin  <https://orcid.org/0000-0003-3947-1072>
 A. Coustenis  <https://orcid.org/0000-0003-3414-3491>

References

- Acton, C., Bachman, N., Semenov, B., & Wright, E. 2018, *P&SS*, **150**, 9
 Ádámkóvics, M., de Pater, I., Hartung, M., & Barnes, J. W. 2009, *P&SS*, **57**, 1586
 Ádámkóvics, M., de Pater, I., Roe, H. G., Gibbard, S. G., & Griffith, C. A. 2004, *GeoRL*, **31**, L17S05
 Ádámkóvics, M., Mitchell, J. L., Hayes, A. G., et al. 2016, *Icar*, **270**, 376
 Adriani, A., Moriconi, M., Liberti, G., et al. 2005, *EM&P*, **96**, 109
 Albert, S., Bauerecker, S., Boudon, V., et al. 2009, *CP*, **356**, 131
 Anderson, C. M., Samuelson, R. E., Achterberg, R. K., Barnes, J. W., & Flasar, F. M. 2014, *Icar*, **243**, 129
 Barnes, J. W., Brown, R. H., Soderblom, L., et al. 2007, *Icar*, **186**, 242
 Barnes, J. W., Brown, R. H., Soderblom, L., et al. 2008, *Icar*, **195**, 400
 Barnes, J. W., Lorenz, R. D., Radebaugh, J., et al. 2015, *PiSci*, **4**, 1
 Barnes, J. W., MacKenzie, S. M., Young, E. F., et al. 2018, *AJ*, **155**, 264
 Barnes, J. W., Turtle, E. P., Trainer, M. G., et al. 2021, *PSJ*, **2**, 130
 Bates, D. R. 1984, *P&SS*, **32**, 785
 Bézard, B. 2014, *Icar*, **242**, 64
 Bézard, B., Nixon, C., Kleiner, I., & Jennings, D. 2007, *Icar*, **191**, 397
 Bird, M. K., Allison, M., Asmar, S. W., et al. 2005, *Natur*, **438**, 800
 Bonnefoy, L. E., Lucas, A., Hayes, A. G., et al. 2022, *PSJ*, **3**, 201
 Botet, R., Rannou, P., & Cabane, M. 1997, *ApOpt*, **36**, 8791
 Boudon, V., Rey, M., & Loete, M. 2006, *JQSRT*, **98**, 394
 Brossier, J. F., Rodriguez, S., Cornet, T., et al. 2018, *JGRE*, **123**, 1089
 Brown, R. H., Baines, K. H., Bellucci, G., et al. 2004, *SSRv*, **115**, 111
 Buras, R., Dowling, T., & Emde, C. 2011, *JQSRT*, **112**, 2028
 Cabane, M., Chassefiere, E., & Israel, G. 1992, *Icar*, **96**, 176
 Cabane, M., Rannou, P., Chassefiere, E., & Israel, G. 1993, *P&SS*, **41**, 257
 Campargue, A., Wang, L., Mondelain, D., et al. 2012, *Icar*, **219**, 110
 Clark, R. N., Brown, R. H., Lytle, D. M., & Hedman, M. 2018, The VIMS Wavelength and Radiometric Calibration 19, Final Report, Version 2.0 NASA Planetary Data System
 Combe, J.-P., Le Mouélic, S., Sotin, C., et al. 2008, *P&SS*, **56**, 951
 Combe, J.-P., McCord, T. B., McFadden, L. A., et al. 2015, *Icar*, **259**, 53
 Corlies, P., McDonald, G. D., Hayes, A. G., et al. 2021, *Icar*, **357**, 114228
 Cornet, T., Rodriguez, S., Maltagliati, L., et al. 2017, *EGUGA*, **19**, 12298
 Coustenis, A., Jennings, D. E., Achterberg, R. K., et al. 2016, *Icar*, **270**, 409
 Coustenis, A., Jennings, D. E., Achterberg, R. K., et al. 2020, *Icar*, **344**, 113413
 Coutelier, M., Cordier, D., Seignovert, B., et al. 2021, *Icar*, **364**, 114464
 De Bergh, C., Courtin, R., Bézard, B., et al. 2012, *P&SS*, **61**, 85
 De Kok, R., Irwin, P. G. J., Teanby, N. A., et al. 2007, *Icar*, **186**, 354
 Doose, L. R., Karkoschka, E., Tomasko, M. G., & Anderson, C. M. 2016, *Icar*, **270**, 355
 Evans, K. F. 2007, *JatS*, **64**, 3854
 Faulk, S. P., Mitchell, J. L., Moon, S., & Lora, J. M. 2017, *NatGe*, **10**, 827
 Flasar, F. M. 1983, *Sci*, **221**, 55
 Fulchignoni, M., Ferri, F., Angrilli, F., et al. 2005, *Natur*, **438**, 785
 Griffith, C. A., Doose, L., Tomasko, M. G., Pentead, P. F., & See, C. 2012, *Icar*, **218**, 975
 Griffith, C. A., Owen, T., Geballe, T. R., Rayner, J., & Rannou, P. 2003, *Sci*, **300**, 628
 Griffith, C. A., Owen, T., & Wagener, R. 1991, *Icar*, **93**, 362
 Gurwell, M. A. 2004, *ApJL*, **616**, L7
 Gurwell, M. A., & Muhleman, D. O. 2000, *Icar*, **145**, 653
 Hanel, R., Conrath, B., Flasar, F. M., et al. 1981, *Sci*, **212**, 192
 Hirtzig, M., Bézard, B., Lellouch, E., et al. 2013, *Icar*, **226**, 470
 Jacquinet-Husson, N., Crepeau, L., Armante, R., et al. 2011, *JQSRT*, **112**, 2395
 Jennings, D. E., Tokano, T., Cottini, V., et al. 2019, *ApJL*, **877**, L8
 Karkoschka, E., & Schröder, S. E. 2016, *Icar*, **270**, 307
 Karkoschka, E., Schröder, S. E., Tomasko, M. G., & Keller, H. U. 2012, *P&SS*, **60**, 342
 Karkoschka, E., & Tomasko, M. G. 2010, *Icar*, **205**, 674
 Karkoschka, E., Tomasko, M. G., Doose, L. R., et al. 2007, *P&SS*, **55**, 1896
 Kazeminejad, B., Atkinson, D. H., & Lebreton, J.-P. 2011, *AdSpR*, **47**, 1622
 Khare, B. N., Sagan, C., Thompson, W. R., et al. 1984, *AdSpR*, **4**, 59
 Kurucz, R. L. 2005, *MSAIS*, **8**, 189, <https://articles.adsabs.harvard.edu/full/2005MSAIS...8...14K/0000014.000.html>
 Lafferty, W. J., Solodov, A. M., Weber, A., Olson, W. B., & Hartmann, J.-M. 1996, *ApOpt*, **35**, 5911
 Lavvas, P., Sander, M., Kraft, M., & Imanaka, H. 2011, *ApJ*, **728**, 80
 Le Gall, A., Janssen, M. A., Paillou, P., Lorenz, R. D., & Wall, S. D. 2010, *Icar*, **207**, 948
 Le Mouélic, S., Cornet, T., Rodriguez, S., et al. 2012, *P&SS*, **73**, 178
 Le Mouélic, S., Cornet, T., Rodriguez, S., et al. 2019, *Icar*, **319**, 121
 Le Mouélic, S., Langevin, Y., & Erard, S. 1999, *JGR*, **104**, 3833
 Le Mouélic, S., Paillou, P., Janssen, M. A., et al. 2008, *JGRE*, **113**, E04003
 Lellouch, E., Bézard, B., Flasar, F. M., et al. 2014, *Icar*, **231**, 323
 Lellouch, E., Coustenis, A., Sebag, B., et al. 2003, *Icar*, **162**, 125
 Li, L., & Mustard, J. F. 2003, *JGRE*, **108**, 5053
 Lopes, R. M. C., Wall, S. D., Elachi, C., et al. 2019, *SSRv*, **215**, 33
 Lorenz, R. D., MacKenzie, S. M., Neish, C. D., et al. 2021, *PSJ*, **2**, 24
 Lorenz, R. D., Turtle, E. P., Barnes, J. W., et al. 2018, *JHATD*, **34**, 374, https://dragonfly.jhuapl.edu/News-and-Resources/docs/34_03-Lorenz.pdf
 Loria, S. 1909, *AnP*, **334**, 605
 Lunine, J. I., Stevenson, D. J., & Yung, Y. L. 1983, *Sci*, **222**, 1229
 Malaska, M. J., Lopes, R. M. C., Williams, D. A., et al. 2016, *Icar*, **270**, 130
 Maltagliati, L., Bézard, B., Vinatier, S., et al. 2015a, *Icar*, **248**, 1
 Maltagliati, L., Rodriguez, S., Sotin, C., et al. 2015b, *EPSC*, **10**, EPSC2015-687, <https://meetingorganizer.copernicus.org/EPSC2015/EPSC2015-687.pdf>
 Markwardt, C. B. 2009, in *ASP Conf. Ser.* 411, *Astronomical Data Analysis Software and Systems XVIII*, ed. D. A. Bohlender, D. Durand, & P. Dowler (San Francisco, CA: ASP)
 Mathé, C., Vinatier, S., Bézard, B., et al. 2020, *Icar*, **344**, 113547
 McCord, T. B., Hayne, P., Combe, J.-P., et al. 2008, *Icar*, **194**, 212
 McKay, C. P., Pollack, J. B., & Courtin, R. 1989, *Icar*, **80**, 23
 McKellar, A. R. W. 1989, *Icar*, **80**, 361
 Meakin, P. 1984, *PhRvA*, **29**, 997
 Menard-Bourcin, F., Menard, J., & Boursier, C. 2007, *JMoSp*, **242**, 55
 Molter, E. M., Nixon, C. A., Cordiner, M. A., et al. 2016, *AJ*, **152**, 42
 Naus, H., & Ubachs, W. 2000, *OptL*, **25**, 347
 Negrão, A., Coustenis, A., Lellouch, E., et al. 2006, *P&SS*, **54**, 1225
 Neish, C. D., Barnes, J. W., Sotin, C., et al. 2015, *GeoRL*, **42**, 3746
 Neish, C. D., Lorenz, R. D., Turtle, E. P., et al. 2018, *ASBio*, **18**, 571
 Niemann, H. B., Atreya, S. K., Demick, J. E., et al. 2010, *JGRE*, **115**, E12006
 Nikitin, A., Brown, L. R., Féjard, L., Champion, J. P., & Tyuterev, V. 2002, *JMoSp*, **216**, 225
 Nikitin, A. V., Brown, L. R., Sung, K., et al. 2013, *JQSRT*, **114**, 1
 Nikitin, A. V., Champion, J.-P., & Brown, L. R. 2006, *JMoSp*, **240**, 14
 Nixon, C. A., Temelso, B., Vinatier, S., et al. 2012, *ApJ*, **749**, 159
 Peck, E. R., & Khanna, B. N. 1966, *JOSA*, **56**, 1059
 Pentead, P. F., & Griffith, C. A. 2010, *Icar*, **206**, 345
 Pollack, J. B., & McKay, C. P. 1985, *JatS*, **42**, 245
 Rannou, P., Cabane, M., Botet, R., & Chassefiere, E. 1997, *JGR*, **102**, 10997
 Rannou, P., Cabane, M., Chassefiere, E., et al. 1995, *Icar*, **118**, 355
 Rannou, P., Cours, T., Le Mouélic, S., et al. 2010, *Icar*, **208**, 850
 Rannou, P., Coutelier, M., Rey, M. M., & Vinatier, S. 2022, *A&A*, **666**, A140
 Rannou, P., Coutelier, M., Riviere, E., et al. 2021, *ApJ*, **922**, 239
 Rannou, P., McKay, C. P., & Lorenz, R. D. 2003, *P&SS*, **51**, 963
 Rannou, P., Toledo, D., Lavvas, P., et al. 2016, *Icar*, **270**, 291
 Rey, M., Nikitin, A. V., Bézard, B., et al. 2018, *Icar*, **303**, 114
 Rodriguez, S., Es-Sayeh, M., Cornet, T., et al. 2021, *AGUFM*, **P45G**
 Rodriguez, S., Le Mouélic, S., Barnes, J. W., et al. 2018, *NatGe*, **11**, 727
 Rodriguez, S., Le Mouélic, S., Sotin, C., et al. 2006, *P&SS*, **54**, 1510
 Rollefson, R., & Havens, R. 1940, *PhRv*, **57**, 710
 Rothman, L. S., Gordon, I. E., Babikof, Y., et al. 2013, *JQSRT*, **130**, 4
 Schinder, P. J., Flasar, F. M., Marouf, E. A., et al. 2020, *Icar*, **345**, 113720
 Schroder, S. E., & Keller, H. U. 2008, *P&SS*, **56**, 753
 Schröder, S. E., & Keller, H. U. 2009, *P&SS*, **57**, 1963
 Serigano, J., Nixon, C. A., Cordiner, M. A., et al. 2016, *ApJL*, **821**, L8
 Smith, P. L., Huber, M. C. E., & Parkinson, W. H. 1976, *PhRvA*, **13**, 1422
 Snee, M., & Ubachs, W. 2005, *JQSRT*, **92**, 293
 Soderblom, J. M., Brown, R. H., Soderblom, L. A., et al. 2010, *Icar*, **208**, 905

- Soderblom, L. A., Kirk, R. L., Lunine, J. I., et al. 2007, [P&SS](#), **55**, 2025
- Solomonidou, A., Coustenis, A., Hirtzig, M., et al. 2016, [Icar](#), **270**, 85
- Solomonidou, A., Coustenis, A., Lopes, R. M. C., et al. 2018, [JGRE](#), **123**, 489
- Solomonidou, A., Hirtzig, M., Coustenis, A., et al. 2014, [JGRE](#), **119**, 1729
- Solomonidou, A., Neish, C., Coustenis, A., et al. 2020, [A&A](#), **641**, A16
- Sotin, C., Jaumann, R., Buratti, B. J., et al. 2005, [Natur](#), **435**, 786
- Sylvestre, M., Teanby, N. A., Vatan d'Ollone, J., et al. 2020, [Icar](#), **344**, 113188
- Teanby, N. A., Bézard, B., Vinatier, S., et al. 2017, [NatCo](#), **8**, 1586
- Teanby, N. A., Sylvestre, M., Sharkey, J., et al. 2019, [GeoRL](#), **46**, 3079
- Thelen, A. E., Nixon, C. A., Chanover, N. J., et al. 2019, [Icar](#), **319**, 417
- Tomasko, M. G., Doose, L., Engel, S., et al. 2008, [P&SS](#), **56**, 669
- Vinatier, S., Bézard, B., Lebonnois, S., et al. 2015, [Icar](#), **250**, 95
- Vinatier, S., Bézard, B., & Nixon, C. A. 2007, [Icar](#), **191**, 712
- Vinatier, S., Bézard, B., Nixon, C. A., et al. 2010, [Icar](#), **205**, 559
- Vinatier, S., Mathé, C., Bézard, B., et al. 2020, [A&A](#), **641**, A116
- Vinatier, S., Rannou, P., Anderson, C. M., et al. 2012, [Icar](#), **219**, 5
- Werynski, A., Neish, C. D., Gall, A. L., & Janssen, M. A. 2019, [Icar](#), **321**, 508
- Yelle, R. V., Koskinen, T. T., & Palmer, M. Y. 2021, [Icar](#), **368**, 114587
- Yung, Y. L., Allen, M., & Pinto, J. P. 1984, [ApJS](#), **55**, 465